



# Formation Design of Distributed Telescopes in Earth Orbit for Astrophysics Applications

Adam W. Koenig,\* Bruce Macintosh,<sup>†</sup> and Simone D'Amico<sup>‡</sup>

*Stanford University, Stanford, California 94305*

DOI: 10.2514/1.A34420

This paper presents a new formation design that enables deployment of large distributed telescopes aligned with inertial targets in Earth orbit. To minimize propellant consumption, the proposed design uses a two-phase operations concept including observations and formation reconfigurations. During observations, a quasi-continuous control system negates the relative acceleration perpendicular to the line of sight, allowing the interspacecraft separation to passively drift. After each observation, a formation reconfiguration is performed to ensure proper alignment with the target at the start of the next observation. Absolute and relative orbits that minimize the total delta-v cost of a specified mission profile are derived in closed-form including effects of perturbations such as Earth oblateness. Additionally, a new stochastic model predictive control architecture is proposed that uses an optimal impulsive control algorithm to efficiently control the formation. The performance and value of the proposed formation design are demonstrated through high-fidelity simulations of a reference mission to image the exoplanet AEgir using a small starshade and telescope. The results of these simulations demonstrate both that the proposed formation design globally minimizes the delta-v cost of the mission and that the mission is feasible with current propulsion technologies.

## Nomenclature

$a$	= orbit semimajor axis
$B$	= control input matrix
$e$	= orbit eccentricity
$F$	= Fresnel number
$i$	= orbit inclination
$N$	= number of starshade petals
$n$	= orbit mean motion
$P$	= state covariance matrix
$Q$	= process noise matrix
$R$	= starshade radius
$r$	= spacecraft absolute position vector
$T$	= orbit period
$t$	= time
$U$	= maneuver covariance matrix
$\mathbf{x}$	= state vector
$z$	= interspacecraft separation
$\alpha$	= right ascension of target star
$\delta$	= declination of target star
$\epsilon$	= control law parameter
$\theta$	= orbit true argument of latitude
$\lambda$	= wavelength
$\mu$	= Earth gravitational parameter
$\nu$	= orbit true anomaly
$\rho$	= relative position
$\sigma$	= uncertainty parameter
$\Phi$	= state transition matrix
$\Omega$	= orbit right ascension of the ascending node
$\omega$	= orbit argument of perigee

## Subscripts

$N$	= cross-track component
$R$	= radial component
$T$	= along-track component
$\perp$	= component perpendicular to line of sight
$\parallel$	= component parallel to line of sight

## I. Introduction

### A. Motivation

DISTRIBUTED telescopes are an enabling technology for a variety of astrophysics mission concepts. In this paper, a distributed telescope is defined as a group of spacecraft with optical components that work together to act as a single larger instrument. Potential applications for distributed telescopes include solar coronagraphy [1], interferometry [2], and high-contrast imaging [3]. A key advantage of distributed telescopes is that they enable deployment of optical systems that are too large for a monolithic spacecraft. However, distributed telescopes for astrophysics applications must perform maneuvers to maintain precise alignment with inertial targets such as stars, galaxies, or black holes. As a result, the lifetimes of these missions are limited by the available propellant.

To minimize the cost of these missions, it is desirable to deploy distributed telescopes in Earth orbit. This approach enables use of smaller launch vehicles or deployment as a secondary payload. Additionally, communication with the spacecraft is simplified due to reduced distance and more frequent ground contact opportunities. However, the relative accelerations experienced by formations in Earth orbit are multiple orders of magnitude larger than those experienced by formations in deep space. As a result, aligning a formation in Earth orbit with an inertial target for an extended time period without incurring impractical delta-v costs is a challenging problem. A formation design that minimizes the delta-v cost of aligning a formation in Earth orbit with inertial targets is a key enabler for low-cost distributed telescope missions.

A valuable example of such missions is a high-contrast imaging pathfinder that uses a small starshade and telescope to directly image the vicinities of nearby stars. During nominal operations, the telescope images the vicinity of the target star from within the deep shadow produced by the starshade. The objectives of such a mission can be divided into two broad topics: 1) retiring critical formation flying technology gaps [4], and 2) precursor science in service of future flagship missions. Because the formation would be deployed in Earth orbit, the performance of optical navigation systems needed for full-

Received 22 October 2018; revision received 20 February 2019; accepted for publication 31 March 2019; published online 22 May 2019. Copyright © 2019 by Koenig, Macintosh, and D'Amico. Published by the American Institute of Aeronautics and Astronautics, Inc., with permission. All requests for copying and permission to reprint should be submitted to CCC at www.copyright.com; employ the eISSN 1533-6794 to initiate your request. See also AIAA Rights and Permissions www.aiaa.org/randp.

\*Postdoctoral Scholar, Department of Aeronautics and Astronautics, 496 Lomita Mall. Student Member AIAA.

<sup>†</sup>Professor, Department of Physics, 382 Via Pueblo.

<sup>‡</sup>Assistant Professor, Department of Aeronautics and Astronautics, 496 Lomita Mall. Associate Fellow AIAA.

scale missions could be validated through comparison to a reference navigation system (e.g. using Global Navigation Satellite System (GNSS) receivers). Such a mission could also provide a valuable science return by imaging targets with more relaxed optical requirements than Earth analogs. Specifically, the mission could image large, bright exoplanets (i.e., Jupiter analogs) or debris disks surrounding nearby sun-like stars. Images of the debris disks could simultaneously improve estimates of the density of the dust surrounding a “typical” mature star and enable validation of predictions using excess infrared flux from campaigns such as the hunt for observable signatures of terrestrial systems (HOSTS) survey [5].

## B. State of the Art

Studies on design [6–10], guidance [11–13], navigation [14–17], and control [18–22] of spacecraft formations are widely available in the literature. More comprehensive reviews of these studies can be found in recent survey papers [23–26]. However, only a small fraction of these studies address the alignment of a formation with an inertial target. Notable works include studies of probe-class and flagship missions that use starshades to directly image Earth analogs [3,27,28]. However, these studies assume that the formation is deployed in deep space (e.g., in an Earth-leading heliocentric orbit or around the Earth–sun L2 point). Accordingly, formation alignment is maintained by simply negating the relative acceleration between the spacecraft. The delta-v cost incurred by adopting this operations strategy in Earth orbit would be impractical for separations on the order of kilometers or more. Indeed, demonstrations of formation alignment with inertial targets to date, such as the nearby earth astrometric telescope (NEAT) pathfinder experiment on the prototype research instruments and space mission technology advancement mission [29] or the CubeSat Astronomy by NASA and Yonsei using Virtual Telescope Alignment eXperiment mission [30], are limited to separations on the order of tens of meters. Although the European Space Agency’s (ESA’s) planned Proba-3 mission will repeatedly align with the sun at a separation of over 100 m, this mission uses a highly eccentric orbit to reduce the relative acceleration between the spacecraft [10]. Missions such as the proposed starshade pathfinder will require interspacecraft separations that are multiple orders of magnitude larger. To enable such missions without incurring impractically large delta-v costs, it is necessary to develop a formation design specifically for astrophysics applications that require extended periods of fixed inertial alignment at large baseline separations.

## C. Contributions

To meet this need, this paper presents a formation design that enables deployment of large distributed telescopes for astrophysics applications in Earth orbit. The contributions of this paper to the state of the art are threefold. First, an optical analysis is performed to characterize the capabilities of small starshades and telescopes. This analysis is conducted with two objectives:

- 1) Determine benchmark requirements on the interspacecraft separation and integration time that must be accommodated by the formation design;
- 2) Demonstrate that small starshades and telescopes can image scientifically interesting targets.

Second, optimal absolute and relative orbits that minimize the delta-v cost of repeatedly acquiring and maintaining alignment with a specified target including effects of perturbations such as Earth

oblateness  $J_2$  are derived in closed form. Third, a novel multistage navigation and control architecture is developed to ensure that the formation achieves and maintains proper alignment throughout all observations. The backbone of the proposed control architecture is a stochastic model predictive controller that uses a real-time impulsive control solver recently developed by Koenig and D’Amico [31] to minimize propellant consumption at a low computation cost.

These contributions are combined in the analysis and high-fidelity simulation of a reference mission using a small starshade and a telescope in Earth orbit. The operations concept for this mission is described in the following. At launch, the telescope spacecraft is stowed inside the larger starshade spacecraft. The formation is launched as a secondary payload into a readily accessible orbit such as a sun-synchronous low Earth orbit (LEO) or a geosynchronous transfer orbit (GTO). After separation from the launch vehicle, the larger spacecraft performs commissioning operations and deploys the starshade before ejecting the telescope spacecraft. After ejection, the telescope spacecraft performs commissioning operations while the starshade spacecraft acquires the desired nominal separation through a sequence of maneuvers that are also used to calibrate the propulsion system(s). Once the required separation is established, nominal mission operations begin using a two-phase operations concept inspired by ESA’s planned Proba-3 mission [32]. The nominal operations phases include 1) an observation phase during which a quasi-continuous control system keeps the formation precisely aligned with the target by negating the relative acceleration perpendicular to the line of sight (LOS), and 2) a reconfiguration phase during which maneuvers are performed to ensure that the formation is properly aligned at the start of the next observation phase. The geometry of the formation during observations is illustrated in Fig. 1. It is assumed in this paper that the starshade spacecraft performs all maneuvers because its mass, volume, and power margins are expected to be more favorable. However, the proposed formation design can be applied to other architectures (e.g., both spacecraft performing maneuvers) without modification.

The reference mission considered in this paper includes a formation deployed in a GTO that accumulates tens of hours of integration time observing Epsilon Eridani to image the exoplanet AEgir [33] and conduct a detailed analysis of the optical performance of the starshade. The analysis of a similar mission to image debris disks around nearby stars using a formation in LEO can be found in Ref. [34]. In addition to determining the delta-v cost of the nominal mission profile, simulations are conducted to characterize the sensitivity of the delta-v cost to orbit insertion errors. Also, the impact of dynamics, navigation, and control errors are characterized through comparison to ideal reference costs for each observation and reconfiguration phase. Overall, the results of these simulations demonstrate 1) that the proposed navigation and control architecture efficiently controls the formation, 2) that the proposed formation design minimizes the delta-v cost associated with nominal operations, and 3) that the reference mission is feasible with current propulsion technologies for small satellites.

## D. Paper Outline

After this introduction, Sec. II describes the sizing analysis for the optical system to establish baseline requirements for the interspacecraft separation and integration time that must be accommodated by the formation design. Next, Sec. III presents the procedure for

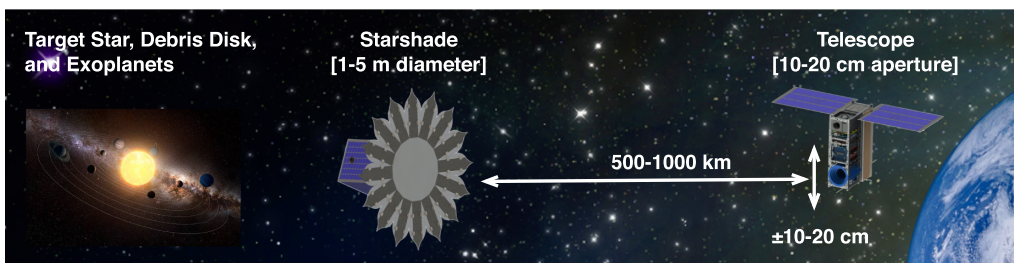


Fig. 1 Illustration of starshade pathfinder mission during an observation phase including relevant dimensions.

**Table 1 Optical model parameters**

Parameter	Value
Bandpass	360–520 nm
Telescope transmission	75%
Quantum efficiency	87%
Read noise	5 e <sup>-</sup> /pixel
Dark current	0.001 e <sup>-</sup> /(pixels · s)
Zodiacal dust	22 magnitudes/arcsec <sup>2</sup>
Exozodiacal dust	21 magnitudes/arcsec <sup>2</sup>

computing optimal absolute and relative orbits for a specified target and observation profile. Section IV describes the proposed navigation and control architecture. Finally, Sec. V describes the simulations of the reference mission profile, and conclusions are discussed in Sec. VI.

## II. Optical Design

Before developing the formation design, it is necessary to first characterize the interspacecraft separation and integration time required for future distributed telescope missions. In this paper, this is accomplished by analyzing the optical system for the proposed high-contrast imaging mission. The analysis presented in the following characterizes two optical design trade spaces for such missions. First, the trade between required integration time and telescope diameter is characterized for both debris disks and large exoplanets. Second, the trade space between the interspacecraft separation, the inner working angle (the minimum angular separation from the star at which an object can be resolved), and the contrast is characterized using conventional starshade analysis and design techniques. More detailed discussions of the proposed starshade design for this mission, including considerations such as manufacturing and deployment errors, can be found in Refs. [34,35].

### A. Telescope Sizing

To minimize the cost of the mission, the telescope should be as small as possible, subject to the constraint that it can meet the requirements of the mission with a reasonable integration time. To characterize the relationship between the telescope size and the required integration time for potential targets of interest, a rigorous optical model was developed that includes telescope transmission, detector quantum efficiency, read noise, dark current, light from zodiacal dust in our solar system, light leakage from the starshade, and light from the debris disk around the target star (for exoplanet computations). The key parameters used in this model are shown in Table 1.

Figure 2 (left) shows the detectable surface brightness (B band) for debris disks for a single 5 min observation using a 10 cm telescope as a function of the apparent magnitude of the host star and the contrast performance of the starshade. The main conclusion that can be drawn from this plot is that disks around most nearby stars with a surface

**Table 2 Potential targets classified as known debris disks (DD), known exoplanets (KP), or potential nearby Earth search (NES)**

Object	B magnitude	Distance, pc	Type	Outer disk size, arcsec
Epsilon Eridani	4.6	3.2	DD, KP, NES	43
Tau Ceti	3.6	3.7	DD, KP, NES	4
Fomalhaut	1.3	7.8	DD, KP	41
HR8799	6.2	40.4	DD, KP	28
Beta Leo	2.2	11.0	DD	7
61 Vir	5.4	8.6	DD	22
Procyon	0.8	3.5	NES	—
Omi 02 Eri	5.9	3.5	NES	—
Alpha Aquillae	1.0	5.1	NES	—
107 Psc	6.1	7.5	NES	—

brightness of almost 22 magnitudes/arcsec<sup>2</sup> can be detected using a CubeSat-compatible telescope as long as the contrast provided by the starshade is  $10^{-7}$  or better. However, several important caveats must be added. The detectability of the disk will depend not only on its total emission but also on its geometry. For example, an extended face-on disk occupies more detector pixels, reducing sensitivity, and may resemble the broad halo of light leaking through the starshade. Also, the plot in Fig. 2 (left) includes only disks that can be detected photometrically by summing all the light over the disk's extent. The resolving structure in the disk in  $N$  distinct regions would increase the exposure time by roughly  $N$ . Still, these calculations show that even moderately bright disks ( $10^{-6}$  relative to host star) will be detectable. Brighter disks may be partially resolved, allowing measurements of the inclination and brightness vs. azimuth.

To detect exoplanets, it is necessary to increase the telescope diameter to ensure reasonable integration times. With this in mind, Fig. 2 (right) shows the required integration time for a 5- $\sigma$  detection of an exoplanet using a 20 cm telescope for a starshade contrast of  $10^{-8}$  plotted against the apparent magnitude (B band) of the host star and the relative brightness of the planet. It is evident that detecting a planet with a relative brightness of  $10^{-9}$  in less than 100 h is infeasible unless it is orbiting one of the brightest stars in the sky. However, planets with a relative brightness of  $10^{-8}$  to  $10^{-7}$  can be detected with tens of hours of integration time, provided that the host star is sufficiently bright. It should be noted that these integration times are only sufficient to detect the planet, and spectroscopic characterization would require considerably longer.

A survey of potential targets of interest was conducted based on the detection capabilities of small telescopes. A selection of identified targets is shown in Table 2. These targets are classified into three categories: 1) known debris disks, 2) known exoplanets, and 3) candidates for a nearby Earth search for future flagship missions. Overall, this survey shows that a range of scientifically interesting targets can be studied using small telescopes. The integration times needed to image these targets range from a few minutes to tens of hours.

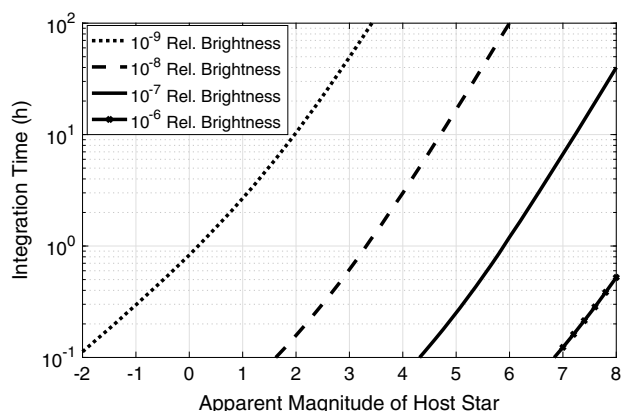
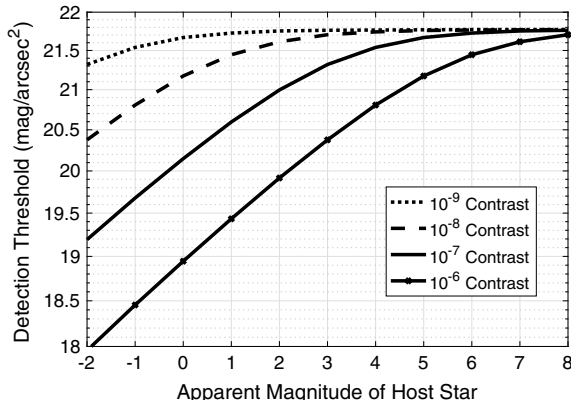


**Fig. 2 Detectable exozodi for 5 min observation using 10 cm telescope vs apparent magnitude of host star and starshade contrast (left) and required integration time for 5- $\sigma$  detection of an exoplanet using 20 cm telescope vs apparent magnitude of host star and relative (Rel.) brightness of planet (right).**

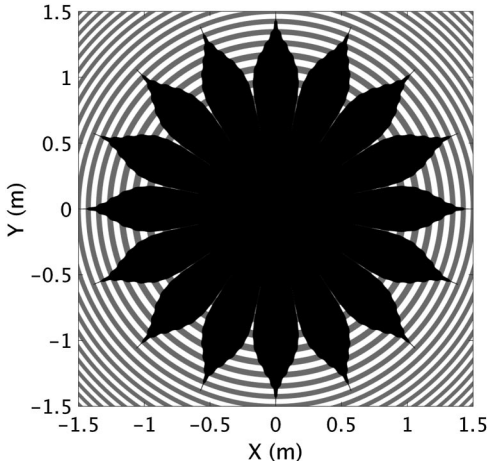


**Fig. 3** Example petal-shaped starshade (black) including Fresnel half-zones (gray and white).

### B. Starshade Sizing

The starshade must be designed to meet two requirements:

- 1) The starshade must produce a sufficiently deep shadow to ensure that diffracted starlight does not compromise collected images;
- 2) The starshade must not block the light from targets of interest.

It has been known for some time that a family of petal-shaped starshades can meet both of these requirements [3,36,37]. An example of this type of starshade is shown in Fig. 3. This design produces a deep shadow by ensuring that the light diffracting around the starshade destructively interferes. In Fig. 3, this is equivalent to ensuring that the gray and white areas (corresponding to opposite phases of the diffracted light passing the starshade) are equal.

Design and analysis techniques for these starshades have been studied extensively for the past 15 years. Indeed, previous authors have studied small-scale starshade designs for laboratory experiments [38], large-scale designs for survey missions to image Earth analogs [3,27,39], and scaling relations using scalar Fresnel theory [40,41]. However, previous authors have largely ignored one-tenth scale (several-meter diameter) starshades because they are simultaneously too large for ground-based experiments and too small for Earth analog imaging missions. To fill this gap, starshades that meet the contrast and inner working angle requirements to image the targets described in Table 2 are identified using a two-step process. First, the search space for useful starshades is bounded through analysis based on conventional starshade scaling relations. Second, starshade designs are computed for a range of points in this search space to verify that these geometries provide sufficiently deep shadows. More detailed analyses of the starshade design including manufacturing and deployment errors as well as sensitivity to numerous design variables can be found in Refs. [34,35].

The performance of a starshade depends on the inner working angle (IWA) and the contrast, which is known to depend on the Fresnel number  $F$ . These parameters are defined as

$$\text{IWA} = \frac{R}{z} \quad F = \frac{R^2}{z\lambda} = \text{IWA} \frac{R}{\lambda} \quad (1)$$

where  $R$  is the starshade radius,  $z$  is the separation between the starshade and telescope, and  $\lambda$  is the wavelength. From previous studies [3,42], the required  $F$  to achieve sufficient contrast to image Earth-like planets is approximately 10. It follows that it is necessary to minimize  $R$  and  $z$  as much as possible while minimizing the impact on  $F$  to enable deployment of a small-scale starshade formation in Earth orbit. It is evident from Eq. (1) that  $F$  is proportional to the IWA and inversely proportional to  $\lambda$ . It follows that the starshade size and interspacecraft separation can be minimized by using the smallest possible wavelength and the largest possible IWA. However, the wavelength cannot be reduced indefinitely because the star must be sufficiently bright in the chosen spectrum to allow the target to be

detected. As such, it is hereafter assumed that the starshade will be designed to work in the B band, which is centered at 440 nm. Next, it is necessary to determine how large the IWA can be such that the starshade can still be used to image targets of interest. All of the targets in Table 2 can be imaged using a starshade with an IWA on the order of hundreds of milliarcseconds. From Eq. (1), this range of inner working angles corresponds to starshade radii of 1–5 m and interspacecraft separations of 200–2000 km to achieve a Fresnel number of 10 in the B band. These starshades easily accommodate the 10–20 cm aperture telescopes identified in the previous section. Also, the interspacecraft separations are small enough to allow the formation to be deployed in Earth orbit.

Next, it is necessary to verify that these starshades produce a deep enough shadow to allow imaging of the targets in Table 2. This is accomplished by computing starshade designs for a number of candidate design points and computing the achievable suppression (the amount of light from the star blocked by the starshade). The starshade designs are computed by solving a modified version of the Vanderbei optimization problem [37] as described in the following. The light passing the starshade is modeled as a plane wave with a complex scalar amplitude  $E_0$  and wavelength  $\lambda$ . The starshade is assumed to have an even number  $N$  of identical petals with shapes defined in terms of an apodization function  $A(r)$ , which denotes the fraction of the arc at radius  $r$  covered by the petal. This apodization satisfies  $0 \leq A(r) \leq 1$  for all  $r \leq R$  and  $A(r) = 0$  for all  $r > R$ . Neglecting the contributions of individual petals (which are known to be small, provided that the starshade has a sufficiently large number of petals), the propagated electric field can be expressed as

$$E(\rho, z, \lambda)$$

$$= E_0 e^{2\pi i z / \lambda} \left( 1 - \frac{2\pi}{i\lambda z} \int_0^R A(r) J_0 \left( \frac{2\pi \rho r}{\lambda z} \right) e^{(\pi i / \lambda z)(r^2 + \rho^2)} r dr \right) \quad (2)$$

where  $z$  is the distance from the starshade, and  $\rho$  is the distance from the optical axis. According to this model, the magnitude of the electric field for each  $\rho$ ,  $z$ , and  $\lambda$  is a convex function of the apodization function at each  $r$ . It follows that the  $A(r)$  that produces the deepest shadow can be computed using standard convex optimization solvers for a specified discretization of the starshade radius. The apodization function is computed by solving the convex optimization problem given by the following:

$$\text{Minimize: } E_{\max}^2$$

subject to:

$$\max(|\mathbb{R}(E(\rho, z, \lambda))|, |\mathbb{I}(E(\rho, z, \lambda))|) < E_{\max} / \sqrt{2}$$

$$0 \leq \rho \leq \rho_{\max} \quad \lambda_{\min} \leq \lambda \leq \lambda_{\max} \quad z_{\min} \leq z \leq z_{\max},$$

$$A(r) = 1 \quad 0 \leq r \leq R_{\text{solid}},$$

$$\frac{dA}{dr}(r) \leq 0 \quad 0 \leq r \leq R,$$

$$\frac{\pi r}{N} \left| \frac{d^2 A}{dr^2}(r) \right| \leq A''_{\max} \quad 0 \leq r \leq R,$$

$$A(r) \leq \frac{N}{\pi} \arcsin \left( \frac{2R_{\text{solid}}}{r} \sin \left( \frac{\pi}{N} \right) \right) \quad 2R_{\text{solid}} \leq r \leq R \quad (3)$$

The first constraint governs the size and depth of the shadow. Specifically, it ensures that the magnitude of the electric field in a cylindrical shadow of radius  $\rho_{\max}$  and length  $z_{\max} - z_{\min}$  is no larger than  $E_{\max}$  for all wavelengths between  $\lambda_{\min}$  and  $\lambda_{\max}$ . The length of the shadow is included in this constraint to allow the formation to passively drift along the line of sight (i.e., no control is applied along the line of sight) during observations to minimize propellant consumption. The second, third, and fourth constraints are adopted directly from the Vanderbei problem and ensure 1) that the starshade center is an opaque disk of radius  $R_{\text{solid}}$ , 2) that the apodization function decreases monotonically to improve structural rigidity of the

**Table 3** Starshade design parameter sets

	<i>R</i> , m									
	1.00	1.25	1.5	1.75	2.00	2.25	2.50	2.75	3.00	—
<i>z</i> <sub>mean</sub> , km	200	400	600	800	1000	1200	1400	1600	1800	2000
<i>ρ</i> <sub>max</sub> , cm	15	30	—	—	—	—	—	—	—	—

petals, and 3) that the curvature of the petals does not exceed a specified threshold  $A''_{\max}$  to ensure that the shape can be machined. The fifth constraint ensures that the petals can be deployed using the two-stage folding system described in Ref. [35].

Starshade designs were computed for each combination of  $R$ ,  $z_{\text{mean}}$ , and  $\rho_{\max}$  in Table 3 such that the Fresnel number is between 1 and 10 and the inner working angle is not greater than 1 arcsec. For these computations,  $z_{\min}$  and  $z_{\max}$  are set at 99 and 101%, respectively, of a baseline separation  $z_{\text{mean}}$ . To maximize the Fresnel number, the starshade is designed to block wavelengths in the B band ( $\lambda_{\min} = 360$  nm and  $\lambda_{\max} = 520$  nm). It is also assumed that  $N$  is 16,  $R_{\text{solid}}$  is equal to  $0.4R$ , and  $A''_{\max}$  is  $2000 \text{ m}^{-1}$ . The starshade designs were computed by solving the optimization problem in Eq. (3) using CVX software [43,44].

The performance of these starshades is assessed by analyzing the suppression (defined as  $E_{\max}^2/E_0^2$ ), which is a metric for the amount of light blocked by the starshade. To enable imaging of the targets in Table 2, the suppression should be  $10^{-7}$  or better. The suppression produced by the computed starshade designs is plotted against the Fresnel number and the shadow radius in Fig. 4 (left). It is evident from this plot that the achievable suppression for a starshade can be approximated as a log-linear function of  $F$ , which is in agreement with Cash's findings for starshades based on hyper-Gaussian functions [41]. For example, a suppression of  $10^{-7}$  requires a Fresnel number between seven and eight, depending on the shadow diameter. These results suggest that it is possible to reduce the Fresnel number up to 20% while maintaining sufficient contrast to image the targets described in Table 2. Also, it was noted that, for each combination of  $R$  and  $z_{\text{mean}}$ , the suppression produced by the starshade design for a 15 cm shadow was always better than the suppression for a 30 cm shadow. This behavior is expected because the constraints for the 15 cm shadow are a subset of the constraints for any larger shadow. Overall, these results demonstrate the existence of a family of 1- to 5-m-diameter starshades with sufficient suppression to enable direct imaging of scientifically interesting targets. These starshades require interspacecraft separations of 200–2000 km, which are small enough to be deployed in Earth orbit.

### III. Orbit Design

To minimize the propellant required for the proposed mission, it is necessary to select absolute and relative orbits for the formation to

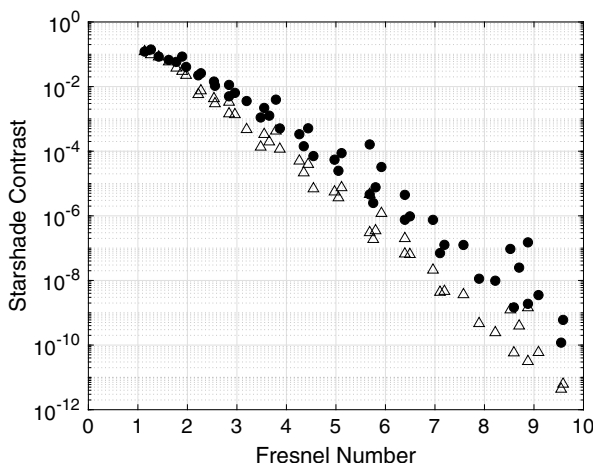


**Fig. 4** Starshade suppression vs Fresnel number (left) for 15 cm shadow radius (triangles) and 30 cm shadow radius (circles).

minimize the combined delta-v costs of 1) maintaining alignment with a target star during observations, and 2) reconfiguring the formation to observe the same target over multiple orbits.

#### A. Observation Phase Analysis

The proposed formation design is based on the assumption that the formation can be allowed to passively drift along the line of sight during observations to save propellant. It follows that the orbit should be selected to ensure that the relative acceleration vector between the spacecraft is (anti)parallel to the relative position vector. With this in mind, it is reasonable to neglect perturbations in the following analysis because they are multiple orders of magnitude weaker than spherical Earth gravity. Let  $\mathbf{r}_{\text{tel}}$  and  $\mathbf{r}_{\text{shade}}$  denote the position vectors of the telescope and starshade, respectively, in the Earth-centered inertial (ECI) frame. Next, let the relative position vector  $\boldsymbol{\rho}$  in the ECI frame be defined as

$$\boldsymbol{\rho} = \mathbf{r}_{\text{shade}} - \mathbf{r}_{\text{tel}} \quad (4)$$

Using these variables, the relative acceleration  $\ddot{\boldsymbol{\rho}}$  between the spacecraft due to spherical Earth gravity is given by

$$\ddot{\boldsymbol{\rho}} = \mu \left( \frac{\mathbf{r}_{\text{tel}}}{\|\mathbf{r}_{\text{tel}}\|^3} - \frac{\mathbf{r}_{\text{shade}}}{\|\mathbf{r}_{\text{shade}}\|^3} \right) = \mu \left( \frac{\mathbf{r}_{\text{tel}}}{\|\mathbf{r}_{\text{tel}}\|^3} - \frac{\mathbf{r}_{\text{tel}} + \boldsymbol{\rho}}{\|\mathbf{r}_{\text{tel}} + \boldsymbol{\rho}\|^3} \right) \quad (5)$$

where  $\mu$  is Earth's gravitational parameter. This relative acceleration can be decomposed into components parallel  $\ddot{\boldsymbol{\rho}}_{\parallel}$  and perpendicular  $\ddot{\boldsymbol{\rho}}_{\perp}$  to the relative position vector as given by

$$\ddot{\boldsymbol{\rho}}_{\parallel} = \frac{\ddot{\boldsymbol{\rho}} \cdot \boldsymbol{\rho}}{\|\boldsymbol{\rho}\|^2} \boldsymbol{\rho} \quad \ddot{\boldsymbol{\rho}}_{\perp} = \ddot{\boldsymbol{\rho}} - \frac{\ddot{\boldsymbol{\rho}} \cdot \boldsymbol{\rho}}{\|\boldsymbol{\rho}\|^2} \boldsymbol{\rho} \quad (6)$$

It is now convenient to consider the relative position vector in the radial/tangential/normal (RTN) frame defined with respect to the telescope spacecraft. In this frame, the radial (R) direction is aligned with the position vector of the telescope spacecraft, the normal (N) direction is aligned with the angular momentum vector, and the tangential (T) direction completes the right-handed triad. The relationships between the position and velocity of the telescope, the relative position vector, the unit pointing vector parallel to the relative position vector  $\hat{\boldsymbol{\rho}}$ , and the components of this pointing vector in the RTN frame are illustrated in Fig. 5. The magnitude of the relative acceleration perpendicular to the LOS, denoted  $\ddot{\boldsymbol{\rho}}_{\perp}$ , can be expressed as a function of these variables as given by

$$\ddot{\boldsymbol{\rho}}_{\perp} = \mu \sqrt{1 - \hat{\boldsymbol{\rho}}_R^2} \left| \frac{\mathbf{r}_{\text{tel}}}{(r_{\text{tel}}^2 + 2\hat{\boldsymbol{\rho}}_R \boldsymbol{\rho} r_{\text{tel}} + \boldsymbol{\rho}^2)^{3/2}} - \frac{1}{r_{\text{tel}}^2} \right| \quad (7)$$

It is evident from Eq. (7) that  $\ddot{\boldsymbol{\rho}}_{\perp}$  is zero if either of two conditions is satisfied: 1)  $|\hat{\boldsymbol{\rho}}_R| = 1$ , or 2)  $\hat{\boldsymbol{\rho}}_R = -0.5\boldsymbol{\rho}/r_{\text{tel}}$ . The first condition means that the formation is aligned in the positive or negative radial direction. To image a specified target, the velocities of the two spacecraft in the ECI frame must be nearly identical. It follows that their specific mechanical energies will be different if the formation is aligned in the radial direction, which means that the orbits must have different semimajor axes. To enable periodic observations, it will be necessary to negate and reestablish this difference in semimajor axes between observations, incurring large delta-v costs. It is therefore evident that a radially aligned formation is not suitable for the proposed mission concept. The second condition is satisfied whenever the telescope and starshade have equal orbit radii. To

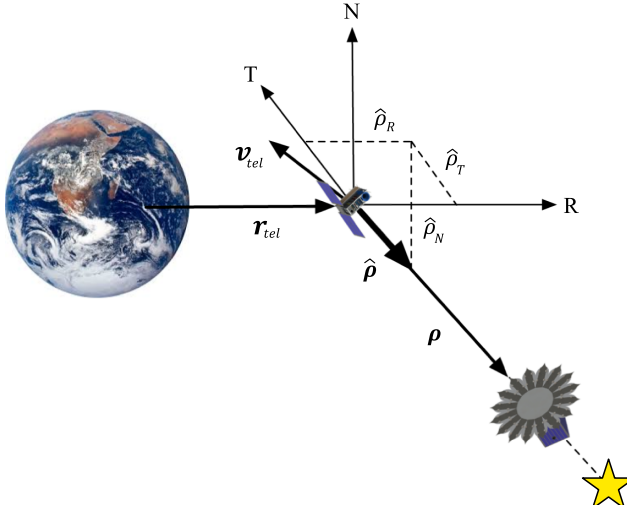


**Fig. 5** Illustration of relationships between the position and velocity of the telescope ( $r_{tel}$  and  $v_{tel}$ ), the relative position vector  $\rho$ , the unit pointing vector parallel to the relative position vector  $\hat{\rho}$ , and the components of the pointing vector in the RTN frame.

minimize propellant consumption, the orbit should be designed to satisfy this condition during observations.

In addition to minimizing the delta-v cost of an observation, it is desirable to maximize the duration over which the formation can be allowed to passively drift along the LOS within a specified separation window. To meet this need, the maximum observation duration and corresponding initial conditions to ensure that the interspacecraft separation remains within a specified margin  $\Delta\rho$  of the baseline are derived in the following. Under the assumption that the spacecraft have equal orbit radii, the magnitude of the relative acceleration in Eq. (5) can be expressed as

$$\ddot{\rho} = -\frac{\mu\rho}{r_{tel}^3} \quad (8)$$

Next, suppose that  $\bar{\rho}$  denotes the baseline interspacecraft separation. If the observation duration  $\Delta t_{obs}$  is small relative to the orbit period (e.g., to ensure that the separation remains within 1% of  $\bar{\rho}$  to be compatible with the starshade designs in Sec. II), the relative acceleration can be approximated as constant. Under this assumption, the separation  $\rho$  between the spacecraft follows the parabolic trajectory given by

$$\rho(t) = \rho(t_i) + \dot{\rho}(t_i)(t - t_i) - \frac{\mu\bar{\rho}}{2r_{tel}^3}(t - t_i)^2 \quad (9)$$

where  $\rho(t_i)$  and  $\dot{\rho}(t_i)$  are the separation and drift velocity at the start of the observation, and the relative acceleration is computed at the baseline separation. To ensure that the telescope remains within the deepest part of the shadow,  $\rho(t_i)$  and  $\dot{\rho}(t_i)$  should be selected to minimize the maximum value of  $|\rho(t) - \bar{\rho}|$  over the observation. Because  $\rho(t)$  follows a parabolic trajectory, the initial conditions that accomplish this are given by

$$\rho(t_i) = \bar{\rho} \left( 1 - \frac{\mu\Delta t_{obs}^2}{16r_{tel}^3} \right) \quad \dot{\rho}(t_i) = \frac{\mu\bar{\rho}\Delta t_{obs}}{2r_{tel}^3} \quad (10)$$

To ensure that the difference between  $\rho(t)$  and  $\bar{\rho}$  never exceeds  $\Delta\rho$  during the observation,  $\Delta t_{obs}$  must satisfy

$$\Delta t_{obs} \leq 4\sqrt{\frac{r_{tel}^3}{\mu}} \frac{\Delta\rho}{\bar{\rho}} \quad (11)$$

It is evident from Eq. (11) that the duration of an observation depends only on the orbit radius and the ratio  $\Delta\rho/\bar{\rho}$ . Assuming that  $\Delta\rho/\bar{\rho}$  is 1% (from Sec. III.B), the maximum observation duration in LEO ( $r_{tel} = 6900$  km, and orbit period of 95 min) is approximately 6 min. This is sufficient to image the debris disks described in Sec. II. However, to image exoplanets that require many hours of integration time, it will be necessary to use a larger orbit such as a GTO (apogee radius of 42,000 km, and orbit period of 10.6 h), which allows observation durations of up to 1.5 h. In both of these cases, the maximum observation duration is small relative to the orbit period, which validates the assumption that the relative acceleration can be approximated as constant.

Now that the maneuver duration and initial conditions have been found, it is necessary to characterize the delta-v cost of an observation. This cost, denoted  $\Delta v_{obs}$ , can be computed by simply integrating the relative acceleration perpendicular to the LOS from Eq. (7) as given by

$$\Delta v_{obs} = \int_{t_0-\Delta t_{obs}/2}^{t_0+\Delta t_{obs}/2} \ddot{\rho}_{\perp}(t) dt \quad (12)$$

However, some simplifying assumptions can be made to render the integral analytically tractable. First, the separation must remain within 1% of the baseline over the complete observation and can be reasonably approximated as constant. Second, because the observation duration must be small relative to the orbit period,  $r_{tel}$  can be approximated as constant during the observation. Under these assumptions, the only time-varying parameter in Eq. (7) is  $\hat{\rho}_R$ . To further simplify the integral, it is helpful to compute a linear approximation of  $\ddot{\rho}_{\perp}$  in the vicinity of the optimal  $\hat{\rho}_R$  as given by

$$\begin{aligned} \ddot{\rho}_{\perp}(\hat{\rho}_R) &= |\hat{\rho}_R + 0.5\bar{\rho}/r_{tel}| \left. \frac{\delta\ddot{\rho}_{\perp}}{\delta\hat{\rho}_R} \right|_{\hat{\rho}_R=-0.5\bar{\rho}/r_{tel}}^+ \\ &= \left| \hat{\rho}_R + \frac{\bar{\rho}}{2r_{tel}} \right| \frac{3\mu\bar{\rho}}{r_{tel}^3} \sqrt{1 - \frac{\bar{\rho}^2}{4r_{tel}^2}} \end{aligned} \quad (13)$$

where the superscript + denotes the positive one-sided derivative, which is necessary to cope with the absolute value in Eq. (7). Substituting Eq. (13) into Eq. (12) yields

$$\Delta v_{obs} = \frac{3\mu\bar{\rho}}{r_{tel}^3} \sqrt{1 - \frac{\bar{\rho}^2}{4r_{tel}^2}} \int_{t_0-\Delta t_{obs}/2}^{t_0+\Delta t_{obs}/2} \left| \hat{\rho}_R(t) + \frac{\bar{\rho}}{2r_{tel}} \right| dt \quad (14)$$

It is evident from this formulation that the cost is minimized by ensuring that  $\hat{\rho}_R$  remains as close as possible to  $-0.5\bar{\rho}/r_{tel}$  over the complete observation. With this in mind, it is instructive to consider the evolution of the unit pointing vector to a star as seen in the RTN frame. If the observation is performed at the apogee of an unperturbed orbit, the evolution of the unit pointing vector to an inertially fixed target in the RTN frame is governed by

$$\frac{d}{dt} \begin{pmatrix} \hat{\rho}_R \\ \hat{\rho}_T \\ \hat{\rho}_N \end{pmatrix} = \frac{\sqrt{\mu(1+e)}}{r_{tel}^{3/2}} \begin{bmatrix} 0 & 1 & 0 \\ -1 & 0 & 0 \\ 0 & 0 & 0 \end{bmatrix} \begin{pmatrix} \hat{\rho}_R \\ \hat{\rho}_T \\ \hat{\rho}_N \end{pmatrix} \quad (15)$$

where  $e$  is the orbit eccentricity. From this equation, it is evident that the rate of change of  $\hat{\rho}_R$  is proportional to  $\hat{\rho}_T$ . It follows that  $|\hat{\rho}_T|$  should be minimized to ensure that  $\hat{\rho}_R$  stays close to its optimal value over the complete observation. In particular, if  $|\hat{\rho}_T|$  is zero, then  $d\hat{\rho}_R/dt$  is zero to the first order. It can also be seen that  $\hat{\rho}_N$  is constant. Because the pointing vector must have unit magnitude, it is possible to specify the ideal choices of  $\hat{\rho}_R$  and  $\hat{\rho}_T$  for a specified  $\hat{\rho}_N$  as given by

$$\begin{aligned} \hat{\rho}_R &= \max \left( -0.5\bar{\rho}/r_{tel}, -\sqrt{1 - \hat{\rho}_N^2} \right) \\ \hat{\rho}_T &= \pm \sqrt{\max(0, 1 - \hat{\rho}_N^2 - 0.25\bar{\rho}^2/r_{tel}^2)} \end{aligned} \quad (16)$$

From Eq. (15), the time derivative of  $\hat{\rho}_R$  in this configuration is given by

$$\frac{d\hat{\rho}_R}{dt} = \pm \frac{\sqrt{\mu(1+e)} \max(0.1 - \hat{\rho}_N^2 - 0.25\bar{\rho}^2/r_{tel}^2)}{r_{tel}^{3/2}} \quad (17)$$

Next, suppose that the pointing vector takes on the values described in Eq. (16) at time  $t_0$ . Combining Eqs. (16) and (17), the behavior of  $\hat{\rho}_R$  in the vicinity of  $t_0$  can be approximated as

$$\begin{aligned} \hat{\rho}_R(t) &= \max\left(-0.5\bar{\rho}/r_{tel}, -\sqrt{1-\hat{\rho}_N^2}\right) \\ &\pm \frac{\sqrt{\mu(1+e)} \max(0.1 - \hat{\rho}_N^2 - 0.25\bar{\rho}^2/r_{tel}^2)}{r_{tel}^{3/2}} (t - t_0) \end{aligned} \quad (18)$$

Finally, substituting Eq. (18) into Eq. (14) and integrating yields

$$\Delta v_{obs} = \begin{cases} \frac{3\mu^{3/2}\bar{\rho}\Delta t_{obs}^2}{4r_{tel}^{9/2}} \sqrt{(1+e)\left(1-\frac{\bar{\rho}^2}{4r_{tel}^2}\right)\left(1-\hat{\rho}_N^2-\frac{\bar{\rho}^2}{4r_{tel}^2}\right)} : |\hat{\rho}_N| \leq \sqrt{1-\frac{\bar{\rho}^2}{4r_{tel}^2}} \\ \frac{3\mu\bar{\rho}\Delta t_{obs}}{r_{tel}^3} \left(\frac{\bar{\rho}}{2r_{tel}} - \sqrt{1-\hat{\rho}_N^2}\right) \sqrt{1-\frac{\bar{\rho}^2}{4r_{tel}^2}} : |\hat{\rho}_N| > \sqrt{1-\frac{\bar{\rho}^2}{4r_{tel}^2}} \end{cases} \quad (19)$$

where  $r_{tel} = a(1+e)$  at the apogee of the orbit. It is evident from this equation that the delta-v cost of a properly timed observation depends only on  $r_{tel}$ ,  $e$ ,  $\Delta t_{obs}$ ,  $\bar{\rho}$ , and  $\hat{\rho}_N$ . Specifically, it is evident that  $\Delta v_{obs}$  is zero to the first order if the orbit is selected to ensure that  $\hat{\rho}_N^2 = 1 - 0.25\bar{\rho}^2/r_{tel}^2$ . Because  $\bar{\rho}$  is expected to be small relative to  $r_{tel}$ , the optimal  $\hat{\rho}_N$  will be close to  $\pm 1$ , which means that the relative position vector should be established primarily in the cross-track direction. Also, because the corresponding optimal value of  $\hat{\rho}_R$  from Eq. (16) is  $-0.5\bar{\rho}/r_{tel}$ , the spacecraft will have equal orbit radii. It follows that the average angular momentum vector between the optimal telescope and starshade orbits is exactly aligned with the target star.

The cost model in Eq. (19) was validated through comparison to numerical simulations of a formation with a 500 km baseline separation in LEO ( $a = 6900$  km, and  $e = 0$ ) and GTO ( $a = 24,500$  km, and  $e = 0.714$ ). In these simulations, the telescope spacecraft follows an unperturbed Keplerian orbit and control is applied to the starshade spacecraft to negate the relative acceleration perpendicular to the LOS. The duration of each simulation was selected using Eq. (11) for an assumed  $\Delta\rho/\bar{\rho}$  of 1%, and the initial conditions for each simulation were computed from Eq. (10). For optimally timed observations, it was found that the average difference between the costs computed from the simulations and Eq. (19) was only 2%, validating the key modeling assumptions.

To characterize the sensitivity of this cost to alignment errors, the delta-v cost of these observation phase simulations is plotted as a function of the radial and tangential components of the unit pointing

vector to the target in the RTN frame (computed in the middle of the observation) in Fig. 6 for LEO (left) and GTO (right). It is evident from these plots that proper orbit selection can reduce the cost of an observation by more than an order of magnitude. Also, the cost is more than 10 times more sensitive to deviations in  $\hat{\rho}_R$  than  $\hat{\rho}_T$  (note difference in axis scaling). This behavior is expected because the acceleration perpendicular to the LOS only depends on  $\hat{\rho}_R$ . Finally, the maximum deviation between the true separation and  $\bar{\rho}$  for all of these simulations was 5.8 km, or 1.16% of the baseline separation. This suggests that the observation duration should be selected to be slightly shorter than stipulated in Eq. (11) to provide some margin for modeling error. More important, this behavior validates the assumption that it is not necessary to control the relative motion along the LOS during observations.

Overall, these results demonstrate that the delta-v cost of aligning a formation with an inertial target is minimized by ensuring that three criteria are met:

- 1) The orbit radius is maximized;
- 2) Both spacecraft have equal orbit radii;
- 3) The baseline separation is established in the cross-track direction.

## B. Reconfiguration Phase Analysis

Achieving sufficient integration time for detailed characterization of the science targets described in Sec. II will require multiple observation phases over consecutive orbits. As such, it is also necessary to minimize the delta-v cost associated with formation reconfigurations between observations. The maneuvers performed during the reconfiguration phase must negate the combined effects of three phenomena: 1) the change in the relative orbit caused by control input during the previous observation phase, 2) the natural relative dynamics during the reconfiguration, and 3) the rotation of the LOS in the RTN frame due to precession of the absolute orbit [mainly inclination or right ascension of the ascending node (RAAN)].

Because the reconfiguration must counteract the effects of control input during the previous observation, it is reasonable to expect that minimizing the observation phase cost will simultaneously minimize the reconfiguration phase cost. This hypothesis is further supported by the following reasoning. To enable repeated observations of the same target, the relative motion of the formation should be nearly periodic. This is only possible if the spacecraft orbits have the same time-averaged semimajor axis. It follows that any difference in the semimajor axis required to observe a specified target (i.e., because  $\hat{\rho}_R \neq -0.5\bar{\rho}/r_{tel}$ ) must be negated and reestablished between observations. Thus, an optimal orbit must ensure that both orbits have equal semimajor axes at the beginning and end of each observation. Because the relative velocity between the spacecraft must be near zero during observations, this means that the orbit radii must be equal. This is equivalent to one of the requirements to minimize the cost of an observation phase.

Next, consider the rotation of the LOS in the RTN frame between observations due to precession of the absolute orbit. If the inclination or RAAN of the spacecraft orbits is affected by perturbations (e.g.,  $J_2$  or solar radiation pressure), it will be necessary to perform maneuvers between observations that adjust the relative motion so the formation

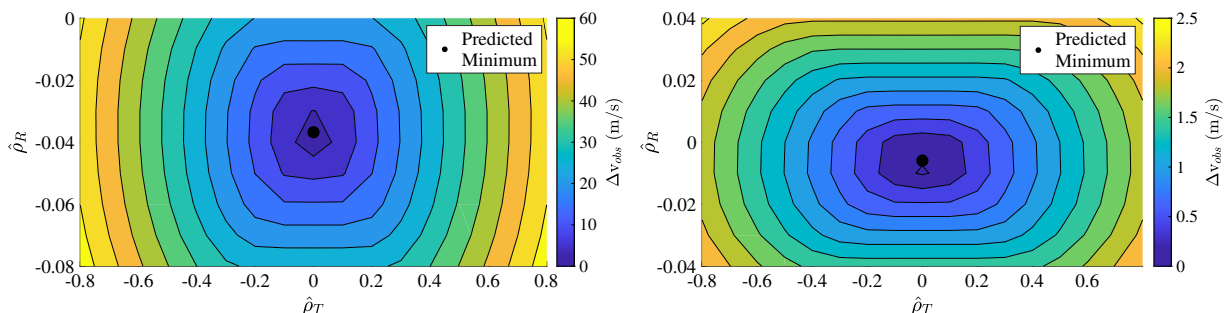


Fig. 6 Numerically integrated delta-v costs for maximum duration observation maneuvers in LEO ( $a = 6900$  km,  $e = 0$ ; left) and GTO ( $a = 24,500$  km,  $e = 0.714$ ; right) for formation with 500 km baseline separation and 1% separation tolerance.

stays aligned with the target star. If the relative position vector in the RTN frame must be rotated by an angle  $\psi$ , then the required delta-v cost  $\Delta v_{\text{rotate}}$  can be approximated as

$$\Delta v_{\text{rotate}} = \frac{\bar{\rho}\psi}{T} \quad (20)$$

The most significant perturbations that can affect the inclination and RAAN in Earth orbit are  $J_2$ , solar radiation pressure, and third-body gravity from the sun and moon. Although the effects of these perturbations depend on the orbit size, separation, and differential ballistic properties, their effects on the orbit of a spacecraft do not exceed 1 deg (0.017 rad) per orbit. It follows that it is reasonable to assume  $\psi$  is 1 deg to approximate the delta-v cost of a single formation reconfiguration. Also, the orbit period can be approximated as 1.5 h for LEO and 10.6 h for GTO. If the baseline separation is assumed to be 500 km, the delta-v cost of a formation reconfiguration according to Eq. (20) is 1.62 m/s for LEO and 0.23 m/s for GTO. By comparing these costs to those in Fig. 6, it is evident that any potential delta-v savings obtained by designing the orbit to minimize the reconfiguration phase cost is negligible as compared to the corresponding increase in the observation phase cost. Overall, this analysis supports the hypothesis that minimizing the observation phase cost simultaneously minimizes the cost of formation reconfigurations for repeated observations.

### C. Minimizing Perturbation Effects

Thus far, it has been demonstrated that the delta-v costs of observation maneuvers and formation reconfigurations are minimized if the orbit radius is maximized. This means that the observation phase should be centered at the apogee of the orbit and the apogee radius should be as large as possible. Additionally, the formation should be aligned in the cross-track direction when observations are performed (specifying inclination and RAAN).

Next, it is necessary to account for the effects of perturbations on the absolute orbit of the formation. The effects of perturbations on the delta-v cost of a mission are minimized if the initial orbit is selected to satisfy two criteria. First, the inclination and RAAN must be centered about their optimal values over the expected mission lifetime to minimize the deviation of the relative motion from the optimal configuration. The optimal initial inclination of the RAAN can be computed by backpropagating the optimal orbit for one-half of the mission lifetime including the dominant perturbations for the specified orbit (e.g.,  $J_2$  for low Earth orbits, and solar radiation pressure and third-body gravity for geosynchronous orbits). Second, the initial orbit must be selected so that the pointing vector to the target in the RTN frame evolves in the (anti)flight direction to ensure that the spacecraft maintain equal orbit energies (see Fig. 6). This can be accomplished by properly selecting the argument of latitude  $\theta$  when observations are performed (or the argument of perigee  $\omega$  for an eccentric orbit). In the general case,  $\theta$  should be selected such that the time derivative of the angular momentum vector is (anti) parallel to the flight direction during observations.

To illustrate this approach, consider a formation in GTO, for which the dominant perturbation is Earth oblateness  $J_2$ . This perturbation causes a secular drift in the RAAN and does not affect the inclination. As a result, the angular momentum vector of the orbit maintains a constant declination as it precesses about Earth's axis. It follows that, if observations are performed at the extreme latitudes ( $\theta = 90$  or 270 deg), then the precession of the RAAN will cause the pointing vector to the target to evolve in the (anti)flight direction [see Eq. (15)]. On the other hand, if observations are performed at the nodes ( $\theta = 0$  or 180 deg), then the pointing vector to the target will evolve in the radial direction, increasing the costs of both observation and reconfiguration phases.

It should be noted that the sensitivity of the delta-v cost of a mission to changes in  $\theta$  will be proportional to the total change in the inclination and RAAN over the mission lifetime. For short missions (where the angular momentum vector rotates no more than a few degrees), it may be more beneficial to select the observation location to simplify mission operations. For example, the argument of latitude

can be selected to ensure that the perigee is above a ground station or to ensure that observations are performed when the formation is in Earth's shadow to prevent scattered sunlight from degrading collected images.

### D. Optimal Orbit Computation

Combining these results, the optimal orbits for a binary distributed telescope at the start of the first observation phase for a mission profile consisting of  $N_{\text{obs}}$  observations of a specified target can be computed using the simple closed-form procedure described in the following. First, an optimal reference orbit is computed. The semimajor axis and eccentricity are determined based on the required integration time for the target. The inclination and right ascension are selected so that the angular momentum vector is (anti)parallel to the pointing vector to the target star. If  $\delta$  and  $\alpha$  denote the declination and right ascension of the target star, then the candidate optimal inclination  $i_{\text{ref}}$  and RAAN  $\Omega_{\text{ref}}$  are given by

$$\begin{pmatrix} i_{\text{ref}} \\ \Omega_{\text{ref}} \end{pmatrix} = \begin{pmatrix} \alpha + \pi/2 \\ \pi/2 - \delta \end{pmatrix} \quad \text{or} \quad \begin{pmatrix} \delta + \pi/2 \\ \alpha - \pi/2 \end{pmatrix} \quad (21)$$

The mean anomaly is specified as  $M_{\text{ref}} = \pi - n\Delta t_{\text{obs}}/2$ , where  $n$  is the mean motion of the orbit. The argument of perigee  $\omega_{\text{ref}}$  can be selected to minimize the delta-v cost incurred by orbit precession or simplify mission operations. Next, the drift rates of the inclination, RAAN, and argument of perigee are computed for the dominant perturbations affecting the orbit. These drift rates are used to backpropagate the orbit orientation so that it is centered about the optimal configuration over the expected mission lifetime. The corresponding initial orbit elements, denoted by subscript  $i$ , are given by

$$\begin{aligned} i_i &= i_{\text{ref}} - \dot{i}T(N_{\text{obs}} - 1)/2 & \Omega_i &= \Omega_{\text{ref}} - \dot{\Omega}T(N_{\text{obs}} - 1)/2 \\ \omega_i &= \omega_{\text{ref}} - \dot{\omega}T(N_{\text{obs}} - 1)/2 \end{aligned} \quad (22)$$

where  $T$  is the orbit period. Third, the position  $\mathbf{r}_{\text{ref}}(t_i)$  and velocity  $\mathbf{v}_{\text{ref}}(t_i)$  of the reference orbit are computed from the initial orbit elements. Finally, the initial position and velocity of each spacecraft (e.g., a telescope and starshade) are computed as given by

$$\begin{aligned} \begin{pmatrix} \mathbf{r}_{\text{tel}}(t_i) \\ \mathbf{v}_{\text{tel}}(t_i) \end{pmatrix} &= \begin{pmatrix} \mathbf{r}_{\text{ref}}(t_i) - \rho(t_i)\hat{\mathbf{e}}_{\text{star}}/2 \\ \mathbf{v}_{\text{ref}}(t_i) - \dot{\rho}(t_i)\hat{\mathbf{e}}_{\text{star}}/2 \end{pmatrix} \\ \begin{pmatrix} \mathbf{r}_{\text{occ}}(t_i) \\ \mathbf{v}_{\text{occ}}(t_i) \end{pmatrix} &= \begin{pmatrix} \mathbf{r}_{\text{ref}}(t_i) + \rho(t_i)\hat{\mathbf{e}}_{\text{star}}/2 \\ \mathbf{v}_{\text{ref}}(t_i) + \dot{\rho}(t_i)\hat{\mathbf{e}}_{\text{star}}/2 \end{pmatrix} \end{aligned} \quad (23)$$

where  $\hat{\mathbf{e}}_{\text{star}}$  is the unit pointing vector to the target star in the ECI frame, and  $\rho(t_i)$  and  $\dot{\rho}(t_i)$  are computed from Eq. (10).

## IV. Navigation and Control Architecture

To demonstrate the feasibility of the proposed small-scale starshade formation in Earth orbit, it is necessary to develop a navigation and control architecture that is capable of meeting the mission requirements. Specifically, it is necessary to develop control laws that 1) keep the telescope within the shadow produced by the starshade (10–20 cm control window) throughout all observations, 2) ensure that the separation is within 1% of the baseline throughout all observations, and 3) reconfigure the formation to ensure proper alignment with a specified target at the start of each observation. The navigation and control architecture described in the following is inspired by the planned approach for full-scale missions using combinations range and range-rate measurements from an intersatellite link (ISL) and differential bearing angles from optical sensors [3]. This architecture can be used in any Earth orbit because it does not rely on carrier-phase differential GNSS techniques, enabling both of the mission concepts described in Sec. I.

**Table 4** 3-5 state estimate uncertainties for proposed navigation metrologies

	Position, m	Velocity, m/s	Useful range
GNSS			
Absolute	100	0.1	Any
Relative	100	0.1	Any
Longitudinal			
RF	10	0.1	Any
Lateral			
Star tracker [45]	25	0.01	$\leq 50$ km
Telescope	0.1	0.002	$\leq 750$ m
Diffracted images	0.01	0.005	$\leq 1.5$ m

### A. Navigation

The navigation concept is based on four sensors: 1) a GNSS receiver on each spacecraft, 2) an ISL that provides range and range-rate measurements, 3) a star tracker on the telescope spacecraft, and 4) a navigation sensor in the telescope. It is assumed that coarse absolute and relative orbit knowledge will be available at all times using the GNSS receivers, as demonstrated by NASA's Magnetospheric Multiscale Mission, which accomplished navigation using side lobes of the GNSS signals at altitudes over 70 Mm (megameters) [16]. However, the GNSS measurements are insufficient to achieve the required centimeter-level alignment accuracy. To address this limitation, more accurate relative position and velocity measurements will be obtained shortly before and during each observation phase by fusing range and range-rate measurements from the ISL with differential bearing angles from the optical sensors as planned for full-scale missions [3]. When the angular separation between the starshade and target is several degrees, the differential bearing angles are provided by a star tracker on the telescope spacecraft. For a sensor similar to the Blue Canyon Technologies Nano Star Tracker, it is expected that the differential bearing angles can be computed with an accuracy of approximately 10 arcsec [45]. When the angular separation decreases to a few hundred arcseconds, a navigation sensor in the telescope is employed to produce more accurate differential bearing angle measurements. Although the diffraction limit for a 20 cm telescope in the B band is approximately 0.5 arcsec, it is expected that similar image processing techniques to those used on star trackers can be employed to achieve measurement accuracies of a few hundredths of an arcsecond. It is also anticipated that the starshade will be equipped with a beacon that can be observed in a different frequency than the star, allowing the point spread function from each source to be distinguished even when they overlap. Finally, when the telescope enters the shadow produced by the starshade, the diffracted images of the star in a different wavelength than the science instrument are processed to provide measurements with milliarc-second-level accuracy. This corresponds to millimeter-level position errors at the considered separations (hundreds of kilometers), which is sufficient to keep the telescope within a few centimeters of the center of the shadow. The anticipated 3- $\sigma$  uncertainties of state estimates after filtering using these measurements are summarized in Table 4. When the optical metrologies are used, the uncertainty is divided into longitudinal (along the LOS) and lateral (perpendicular to the LOS) components. These values are computed for a baseline separation of 500 km and a starshade diameter of 3 m.

### B. Observation Phase Control

The observation phase control law must be designed to ensure that the telescope remains close to the center of the shadow produced by the starshade for the duration of the observation. Using the proposed operations concept, it is only necessary to control the lateral relative position and velocity during this phase. For simplicity, it is assumed that the lateral relative position and velocity estimates will be computed by fusing the range and range-rate measurements with differential bearing angles computed by processing the diffracted images of the star. It is also assumed that the starshade will be equipped with a propulsion system with sufficiently high thrust that

maneuvers can be approximated as impulsive. Under these assumptions, commanded maneuvers during the observation phase are computed using the bang-off-bang state-space control law described in the following. At each update step, estimates of the telescope position  $\mathbf{r}_{\text{tel}}$  and velocity  $\mathbf{v}_{\text{tel}}$  and the relative position  $\boldsymbol{\rho}$  and velocity  $\dot{\boldsymbol{\rho}}$  are taken from the navigation filter and used to estimate the lateral relative position, velocity, and acceleration as given by

$$\begin{aligned} \boldsymbol{\rho}_{\perp} &= \boldsymbol{\rho} - (\boldsymbol{\rho}^T \hat{\mathbf{e}}_{\text{star}}) \hat{\mathbf{e}}_{\text{star}} & \dot{\boldsymbol{\rho}}_{\perp} &= \dot{\boldsymbol{\rho}} - (\dot{\boldsymbol{\rho}}^T \hat{\mathbf{e}}_{\text{star}}) \hat{\mathbf{e}}_{\text{star}} \\ \ddot{\boldsymbol{\rho}}_{\perp} &= \ddot{\boldsymbol{\rho}} - (\ddot{\boldsymbol{\rho}}^T \hat{\mathbf{e}}_{\text{star}}) \hat{\mathbf{e}}_{\text{star}} \end{aligned} \quad (24)$$

where  $\ddot{\boldsymbol{\rho}}$  is computed using Eq. (5). Additionally, the projection of the lateral relative position vector onto the lateral relative acceleration vector, denoted  $\rho_{\text{acc}}$ , is computed as given by

$$\rho_{\text{acc}} = \frac{\boldsymbol{\rho}_{\perp}^T \ddot{\boldsymbol{\rho}}_{\perp}}{\|\ddot{\boldsymbol{\rho}}_{\perp}\|} \quad (25)$$

Let  $\epsilon_{\text{obs}}$  denote a user-specified margin and  $\rho_{\perp,\max}$  denote the maximum allowable value of  $\|\boldsymbol{\rho}_{\perp}\|$  as specified by the starshade design. If  $\|\boldsymbol{\rho}_{\perp}\| > (1 - \epsilon_{\text{obs}})\rho_{\perp,\max}$  and  $\dot{\boldsymbol{\rho}}_{\perp}^T \boldsymbol{\rho}_{\perp} \geq 0$  (meaning that the starshade is approaching the edge of the control window), then a maneuver is commanded to negate the lateral relative velocity and slowly drive the telescope back to the center of the control window. The commanded relative velocity is set at the 1- $\sigma$  uncertainty of the lateral relative velocity estimate to minimize delta-v consumption. If  $\rho_{\text{acc}} \geq 0$  (meaning that the relative acceleration will tend to increase  $\|\boldsymbol{\rho}_{\perp}\|$ ), then the commanded maneuver is augmented to ensure that the telescope is driven back to the center of the shadow accounting for the estimated acceleration. This reduces the number of maneuvers required during observations, minimizing the effect of navigation errors on delta-v consumption. If the telescope is not near the edge of the control window but  $\|\dot{\boldsymbol{\rho}}_{\perp}\|$  is over a specified threshold  $\dot{\rho}_{\max}$  (meaning that the formation has a large lateral relative velocity), then a maneuver is commanded to negate the lateral relative velocity. This ensures that the starshade will not leave the control window before the next update of the control law. The process of computing the maneuver command  $\mathbf{u}$  is summarized in Algorithm 1, where  $\sigma_{\perp,\text{vel}}$  denotes the 1- $\sigma$  uncertainty of the lateral relative velocity estimate.

### C. Reconfiguration Phase Control

The control law for the reconfiguration phase is designed to ensure that the relative state at the start of each observation phase is within a specified control window of the optimal initial condition from Eq. (10). This problem is challenging because the control window is very small (centimeter-level perpendicular to the LOS), and the measurements produced by the navigation system have time-varying accuracy and depend strongly on the direction. To address these challenges, a two-phase stochastic model predictive control architecture was developed. In the first stage (called long-term) the control law uses an impulsive control algorithm recently developed by Koenig and D'Amico [31] to update the maneuver plan whenever the propagated error is outside of the 3- $\sigma$  error bounds. This algorithm is selected because it is suitable for real-time implementation and ensures that maneuver plans include no more than six maneuvers. In

**Algorithm 1** Maneuver command computation for observation phase

---

```

If  $\|\boldsymbol{\rho}_{\perp}\| \geq (1 - \epsilon_{\text{obs}})\rho_{\perp,\max}$  and  $\dot{\boldsymbol{\rho}}_{\perp}^T \boldsymbol{\rho}_{\perp} \geq 0$ , then
     $\mathbf{u} \leftarrow -\dot{\boldsymbol{\rho}}_{\perp} - \sigma_{\perp,\text{vel}}(\boldsymbol{\rho}_{\perp}/\|\boldsymbol{\rho}_{\perp}\|)$ 
    If  $\rho_{\text{acc}} \geq 0$  and  $\|\ddot{\boldsymbol{\rho}}_{\perp}\| > 0$ , then
         $\mathbf{u} \leftarrow \mathbf{u} - \sqrt{2\rho_{\text{acc}}/\|\ddot{\boldsymbol{\rho}}_{\perp}\|} \ddot{\boldsymbol{\rho}}_{\perp}$ 
        end if
    else if  $\|\dot{\boldsymbol{\rho}}_{\perp}\| \geq \dot{\rho}_{\max}$ , then
         $\mathbf{u} \leftarrow -\dot{\boldsymbol{\rho}}_{\perp}$ 
    else
         $\mathbf{u} \leftarrow 0$ 
    end if

```

---

the second stage (called short-term), longitudinal (along the LOS) and lateral (perpendicular to the LOS) control are decoupled to minimize the impact of direction-dependent measurement accuracies on the delta-v cost of reaching the control window.

### 1. Long-Term Control

The long-term control phase begins at the end of an observation phase and lasts the majority of the orbit until shortly before the start of the next observation phase. The primary purpose of this control law is to ensure that the formation is aligned with the target to within the precision of the navigation system. This is accomplished by simply propagating the estimated orbits of both spacecraft (from the navigation system model) to the start of the next observation phase, including uncertainty and planned maneuvers at regular intervals. If the desired relative state is outside of the 3- $\sigma$  uncertainty ellipsoid surrounding the propagated relative state, the maneuver plan is updated. Otherwise, the prior maneuver plan is kept and all planned maneuvers are executed until the next update.

The orbit propagation is accomplished by numerically integrating the equations of motion including the  $J_2$  perturbation. This dynamics model was selected because it is simple to implement and is more accurate than closed-form models available in literature for propagation times of under one orbit. The desired orbit of the starshade is computed by adding the initial separation and drift from Eq. (10) to the propagated state of the telescope spacecraft. The propagated and desired relative states are transformed into a relative orbital elements (ROEs) state defined as

$$\begin{aligned} \mathbf{x}_{\text{ROE}} &= a_t \begin{pmatrix} \delta a \\ \delta \lambda \\ \delta e_x \\ \delta e_y \\ \delta i_x \\ \delta i_y \end{pmatrix} \\ &= a_t \begin{pmatrix} (a_s - a_t)/a_t \\ (M_s - M_t) + \eta_t((\omega_s - \omega_t) + \cos(i_t)(\Omega_s - \Omega_t)) \\ e_s \cos(\omega_s) - e_t \cos(\omega_t) \\ e_s \sin(\omega_s) - e_t \sin(\omega_t) \\ i_s - i_t \\ \sin(i_t)(\Omega_s - \Omega_t) \end{pmatrix} \quad (26) \end{aligned}$$

where the subscripts  $s$  and  $t$  denote the orbit elements of the starshade and telescope, and  $\eta_t = \sqrt{1 - e_t^2}$ . The components of the state vector include the relative semimajor axis  $\delta a$ , the relative mean longitude  $\delta \lambda$ , the relative eccentricity vectors  $\delta e_x$  and  $\delta e_y$ , and the relative inclination vectors  $\delta i_x$  and  $\delta i_y$ . This ROE state is selected because existing linear dynamics models in the literature are valid for large separations [46,47]. These models can be used without modification to update the maneuver plan. Next, the covariance for the relative state in ROE space at the start of the next observation phase, denoted  $P(t_f)$ , is computed using the model given by

$$\begin{aligned} P(t_f) &= \Phi(t_f - t_i)P(t_i)\Phi^T(t_f - t_i) + Q(t_f - t_i) \\ &\quad + \sum \Phi(t_f - t_j)B(t_j)U_jB^T(t_j)\Phi^T(t_f - t_j) \quad (27) \end{aligned}$$

In this model,  $P(t_i)$  is the initial covariance defined in ROE space,  $\Phi$  is the state transition matrix,  $Q$  is the process noise matrix,  $B$  is the control input matrix, and  $U_j$  is the covariance matrix for the  $j$ th planned maneuver. The initial covariance in ROE space is computed by performing an unscented transform on the covariance in Cartesian space. The employed state transition matrix was given by D'Amico [46] for unperturbed orbits as

$$\Phi(t_f - t) = \begin{bmatrix} 1 & 0 & 0 & 0 & 0 & 0 \\ -1.5n(t_f - t) & 1 & 0 & 0 & 0 & 0 \\ 0 & 0 & 1 & 0 & 0 & 0 \\ 0 & 0 & 0 & 1 & 0 & 0 \\ 0 & 0 & 0 & 0 & 1 & 0 \\ 0 & 0 & 0 & 0 & 0 & 1 \end{bmatrix} \quad (28)$$

Although more accurate linear models that include the effects of  $J_2$  and differential atmospheric drag are available [47], the effects of these perturbations have no significant impact on the covariance for propagation times of one orbit or less. The control input matrix is derived from Gauss's variational equations [48] as given by

$$B(t_j) = \frac{1}{n} \begin{bmatrix} 2e \sin(\nu)/\eta & 2(1+e \cos(\nu))/\eta & 0 \\ -\frac{2\nu^2}{1+e \cos(\nu)} & 0 & 0 \\ \eta \sin(\theta) & \eta \frac{(2+e \cos(\nu)) \cos(\theta) + e \cos(\omega)}{1+e \cos(\nu)} & \eta \frac{e \sin(\omega)}{\tan(i)} \frac{\sin(\theta)}{1+e \cos(\nu)} \\ -\eta \cos(\theta) & \eta \frac{(2+e \cos(\nu)) \sin(\theta) + e \sin(\omega)}{1+e \cos(\nu)} & -\eta \frac{e \cos(\omega)}{\tan(i)} \frac{\sin(\theta)}{1+e \cos(\nu)} \\ 0 & 0 & \eta \frac{\cos(\theta)}{1+e \cos(\nu)} \\ 0 & 0 & \eta \frac{\sin(\theta)}{1+e \cos(\nu)} \end{bmatrix} \quad (29)$$

where all specified orbit elements are for the telescope spacecraft,  $\nu$  denotes the true anomaly, and  $\theta = \omega + \nu$ . The true anomaly is evaluated at time  $t_j$  under the assumption that the telescope follows an unperturbed orbit. Finally, the process noise matrix and maneuver covariance matrices are defined as

$$\begin{aligned} Q(t_f - t_i) &= (10^{-3}(t_f - t_i))^2 I^{6 \times 6} \\ U_j &= \epsilon_{\text{control}}^2 \begin{bmatrix} u_{j,R}^2 & 0 & 0 \\ 0 & u_{j,T}^2 & 0 \\ 0 & 0 & u_{j,N}^2 \end{bmatrix} \quad (30) \end{aligned}$$

where  $\epsilon_{\text{control}}$  is the 1- $\sigma$  maneuver execution uncertainty; and  $u_{j,R}$ ,  $u_{j,T}$ , and  $u_{j,N}$  are the radial, along-track, and cross-track components of the  $j$ th planned maneuver. This final covariance matrix is used to determine if the desired state  $\mathbf{x}_{\text{ROE},\text{des}}$  is within the 3- $\sigma$  uncertainty ellipsoid surrounding the propagated state  $\mathbf{x}_{\text{ROE},\text{prop}}$  as given by

$$\sqrt{(\mathbf{x}_{\text{ROE},\text{des}} - \mathbf{x}_{\text{ROE},\text{prop}})^T P^{-1}(t_f) (\mathbf{x}_{\text{ROE},\text{des}} - \mathbf{x}_{\text{ROE},\text{prop}})} \leq 3 \quad (31)$$

If this condition is satisfied, the prior maneuver plan is used until the next update step. Otherwise, the maneuver plan is recomputed.

If required, the maneuver plan is updated using the procedure described in the following. First, the orbit of the starshade is propagated to the start of the next observation without any maneuvers. Next, the final states of the telescope and starshade are used to compute the propagated ROE state  $\mathbf{x}_{\text{ROE},\text{prop}}$ . The propagated and desired states are then used to compute a set of impulsive maneuvers that produce the desired reconfiguration at minimum cost. This is accomplished by solving the optimal control problem given by the following:

$$\begin{aligned} \text{Minimize : } & \sum \|\mathbf{u}_j\| \\ \text{subject to } & \mathbf{x}_{\text{ROE},\text{des}} - \mathbf{x}_{\text{ROE},\text{prop}} = \sum \Phi(t_f - t_j)B(t_j)\mathbf{u}_j \quad (32) \end{aligned}$$

where  $\mathbf{u}_j$  are the applied impulsive maneuvers, and  $t_j$  are the corresponding maneuver execution times. The optimal control problem is solved using the algorithm described in Ref. [31], which provides a set of impulsive maneuvers with a total cost within a user-specified threshold of the global minimum in real time. The algorithm is configured to provide a solution with a cost within 1% of the global optimum. The procedure used to update the maneuver plan  $U$  (including all planned maneuvers and execution times) according to this control logic is summarized in Algorithm 2.

**Algorithm 2** Maneuver plan update for long-term control during reconfiguration phase

---



---

```

 $x_{\text{ROE,prop}} \leftarrow$  propagated relative state including maneuvers
 $x_{\text{ROE,des}} \leftarrow$  desired relative state
 $P(t_f) \leftarrow$  propagated covariance including maneuvers

If  $\sqrt{(x_{\text{ROE,des}} - x_{\text{ROE,prop}})^T P^{-1}(t_f)(x_{\text{ROE,des}} - x_{\text{ROE,prop}})} \leq 3$ , then
     $U \leftarrow U$ 
else
     $x_{\text{ROE,prop}} \leftarrow$  propagated relative state without maneuvers
     $U \leftarrow$  solution to optimal control problem in Eq. (32)
end if
```

---



---

## 2. Short-Term Control

The short-term control phase begins shortly before the start of an observation phase and ends at the start of the observation. The control logic must be designed to ensure that the starshade is within the control window at the start of the next observation phase at minimum delta-v cost. During this time, it is expected that the relative position and velocity of the formation will be estimated using range and range-rate measurements from the ISL and differential bearing angles from the optical sensors. The main challenges that must be addressed are that the lateral and longitudinal control windows and measurement accuracies differ by multiple orders of magnitude. With these challenges in mind, the proposed control logic decouples lateral and longitudinal control to minimize the delta-v cost of reaching the control window. A fundamental assumption used in the derivation of this control law is that the relative acceleration experienced by the formation is constant, which is reasonable, provided that the control logic is used for a small fraction of the orbit. Under this assumption, a delta-v optimal formation reconfiguration consists of two maneuvers executed at the beginning and end of the allowed reconfiguration time. The first maneuver ensures that the desired relative position is achieved, and the second maneuver ensures that the desired relative velocity is achieved. As such, at any time leading up to the start of the observation, an optimal maneuver can be planned by considering only the propagated relative position of the spacecraft. This property is exploited in the control logic described in the following.

At every update step, the relative position at the start of the next observation phase  $\rho_{\text{prop}}$  is computed by propagating the orbits of both spacecraft to the start of the next observation phase. The propagation is accomplished by numerically integrating the equations of motion including the  $J_2$  perturbation. Next, the longitudinal (denoted by subscript  $\parallel$ ) and lateral (denoted by subscript  $\perp$ ) position errors at the start of the observation phase are computed as given by

$$\rho_{\text{err},\parallel} = ((\rho_{\text{prop}} - \rho_{\text{des}})^T \hat{\mathbf{e}}_{\text{star}}) \hat{\mathbf{e}}_{\text{star}} \quad \rho_{\text{err},\perp} = (\rho_{\text{prop}} - \rho_{\text{des}}) - \rho_{\text{err},\parallel} \quad (33)$$

where  $\rho_{\text{des}}$  is the desired relative position from Eq. (10). The longitudinal and lateral position uncertainties at the start of the next observation phase  $\sigma_{\text{pos}}(t_f)$  are computed from the current position and velocity estimate uncertainties ( $\sigma_{\text{pos}}$  and  $\sigma_{\text{vel}}$ ) as given by

$$\begin{aligned} \sigma_{\text{pos},\parallel}(t_f) &= \sqrt{\sigma_{\text{pos},\parallel}^2(t) + (t_f - t)^2 \sigma_{\text{vel},\parallel}^2(t)} \\ \sigma_{\text{pos},\perp}(t_f) &= \sqrt{\sigma_{\text{pos},\perp}^2(t) + (t_f - t)^2 \sigma_{\text{vel},\perp}^2(t)} \end{aligned} \quad (34)$$

Using these values, maneuvers are commanded to counteract the longitudinal and/or lateral relative position errors unless one of the following two conditions is met:

- 1) The error is within the  $3\sigma$  uncertainty region;
- 2) The entire  $3\sigma$  uncertainty region is within the control window.

If required, the commanded maneuver is computed by dividing the propagated position error by the time until the start of the next observation phase. The procedure for computing the maneuver command  $\mathbf{u}$  is summarized in Algorithm 3.

**Algorithm 3** Maneuver command for short-term control

---



---

```

If  $\|\rho_{\text{err},\parallel}\| \geq \max(\rho_{\parallel,\text{max}} - 3\sigma_{\text{pos},\parallel}(t_f), 3\sigma_{\text{pos},\parallel}(t_f))$ , then
     $u_{\parallel} = -\rho_{\text{err},\parallel}/(t_f - t)$ 
else
     $u_{\parallel} = 0$ 
end if
If  $\|\rho_{\text{err},\perp}\| \geq \max(\rho_{\perp,\text{max}} - 3\sigma_{\text{pos},\perp}(t_f), 3\sigma_{\text{pos},\perp}(t_f))$ , then
     $u_{\perp} = -\rho_{\text{err},\perp}/(t_f - t)$ 
else
     $u_{\perp} = 0$ 
end if
 $\mathbf{u} = u_{\parallel} + u_{\perp}$ 
```

---



---

Finally, at the start of the observation phase, a maneuver is performed to negate the difference between the estimated and desired relative velocities.

## V. Case Study: AEgir

The performance and value of the proposed formation design are demonstrated through the analysis of a reference mission to image the exoplanet AEgir using a small starshade and telescope deployed in a GTO. An analysis of a similar mission to survey debris disks using a formation in LEO can be found in Ref. [34]. Because use of carrier-phase differential GNSS techniques [49,50] is infeasible at high altitude, this choice also motivates the development of the multistage navigation and control architecture described in the previous section. AEgir was chosen as the target because it has relaxed optical requirements due to its average relative brightness of  $10^{-8}$  and angular separation of 1.05 arcsec from its host star [33,51]. To ensure that the planet can be imaged even in an unfavorable position, the reference mission employs a starshade with a 1.5 m radius and a baseline separation of 500 km for an inner working angle of 0.612 arcsec. Using the mean B-band wavelength of 440 nm, this starshade has a Fresnel number of 10. The geometry for this starshade (illustrated in Fig. 3) was computed by solving the optimization problem in Eq. (3) for a 30 cm shadow radius and a 1% separation tolerance, providing a theoretical suppression of  $10^{-10}$ . However, it is assumed that manufacturing and deployment errors result in a contrast of  $10^{-8}$ . Using the optical model described in Sec. II, a 20 cm telescope will require 44.2 h of integration time to achieve a  $10\sigma$  detection, which is sufficient for a coarse spectral characterization. During these observations, it is necessary to keep the formation aligned with the target to within 20 cm to keep the entire telescope aperture in the deepest part of the shadow produced by the starshade. The formation is deployed in a GTO with a semimajor axis of 24,500 km and an eccentricity of 0.714. This orbit has a period of 10.6 h and an apogee radius of 42,000 km. For this orbit, the required baseline separation of 500 km can be established by one or more maneuvers performed at the semilatus rectum of the orbit (true anomaly of 90 deg). From Gauss's variational equations [48], the total delta-v cost of these maneuvers is 68.6 m/s. The planned observation profile consists of 32 observations of 1.4 h duration to ensure that the separation remains within 1% of the baseline with margin for modeling errors in the drift rate. The argument of perigee is centered about 90 deg over the mission lifetime to minimize the delta-v cost. Using the procedure described in Sec. III, the optimal initial osculating Keplerian orbit elements for the telescope and starshade are given in Table 5.

Table 5 Initial orbits for telescope and starshade spacecraft

Orbit element	$a$ , km	$e$	$i$ , deg	$\Omega$ , deg	$\omega$ , deg	$M$ , deg
Telescope	24500	0.7143	99.80	142.92	91.19	156.23
Starshade	24501	0.7143	99.11	142.91	91.19	156.23

**Table 6 Numerical orbit propagator parameters**

Parameter	Value
Integrator	Runge–Kutta (Dormand–Prince)
Step size	Fixed: 60 s
Geopotential	GGM01S (120 × 120) [53]
Atmospheric density	NRLMSISE-00 [54]
Third-body gravity	Lunar and solar point masses, analytical ephemerides
Solar radiation pressure	Satellite cross section normal to the sun, no eclipses

### A. Simulation Description

The mission is simulated using a high-fidelity orbit propagator that includes all significant perturbations in Earth orbit [52]. The models used for each of these perturbations are summarized in Table 6 [53,54]. The integrator is based on Gauss's variational equations, which allow the time step to be increased to the order of minutes without compromising propagation accuracy.

The mission simulation proceeds by alternately conducting observation and reconfiguration phases. In these simulations, the observation phase control law (Algorithm 1) is implemented every 2 s. After each reconfiguration phase, the long-term control logic for the reconfiguration phase (Algorithm 2) is implemented every hour until 1 h before the start of the next observation phase. The short-term control logic (Algorithm 3) is implemented every 30 s in the hour leading up to the start of each observation phase. Control errors are simulated by applying Gaussian noise (5% at 3- $\sigma$ ) to the magnitude of each planned maneuver. Key parameters for the control laws are included in Table 7. The parameters for the observation phase control law ( $\dot{\rho}_{\perp,\max}$  and  $\epsilon_{\text{obs}}$ ) were selected to ensure that the starshade does not leave the control window before a maneuver is commanded with the worst-case lateral relative velocity.

In addition to the described simulation, an ideal reference cost is computed for each observation and reconfiguration phase to isolate the effects of navigation, control, and dynamics model errors on the delta-v cost of the mission. This reference cost differs from the simulation cost in three respects:

- 1) It is assumed that the ground truth states of both spacecraft are known;
- 2) Orbit propagation is accomplished using the ground truth dynamics model;
- 3) It is assumed that maneuvers are executed exactly as planned.

The reference cost for each observation phase is computed by propagating the orbits of both spacecraft using the high-fidelity propagator and applying continuous control to the starshade that negates the relative acceleration perpendicular to the LOS. It cannot be claimed that the reference cost is optimal because exploitation of the control window could further reduce cost. For example, if the lateral relative velocity and acceleration are very small, it may not be necessary to apply any control input. Nevertheless, this reference cost

provides a reasonable benchmark for the achievable delta-v cost for an observation phase. The reference cost for the reconfiguration phase is computed as follows. First, the orbits of both spacecraft are propagated to the start of the next observation phase using the high-fidelity propagator without any maneuvers. Next, the desired relative state is computed by adding the initial relative position and velocity from Eq. (10) to the position and velocity of the telescope. Finally, the propagated and desired states are used to solve the optimal control problem defined in Eq. (32) using the algorithm described in Ref. [31]. The reference cost for the reconfiguration phase is the sum of the magnitudes of the planned maneuvers. This reference cost provides a lower bound on the delta-v cost of a reconfiguration phase because it is not necessary to correct for navigation and maneuver execution errors over a short time at the end of the reconfiguration phase.

### B. Simulation Results

There are two success criteria for each simulation. First, the magnitude of the lateral relative position vector must not exceed 20 cm throughout all observation phases. Second, the interspacecraft separation must be within  $\pm 1\%$  of the baseline ( $\pm 5$  km) throughout all observation phases. Both of these criteria were met for all conducted simulations.

To characterize the total delta-v cost of the specified mission profile, simulations were conducted for the optimal initial orbits specified in Table 5 and for initial conditions in which the inclination and RAAN are displaced from their optimal values. The combined delta-v costs of all observation and reconfiguration phases for each of these simulations are provided in Table 8. Several conclusions can be drawn from this sensitivity study. First, it is evident that the selected orbit minimizes the delta-v cost of the mission profile within the considered range. By comparing the total costs to the individual observation maneuver costs in Fig. 6 (right), it is evident that this is the global minimum delta-v cost for the specified observation sequence. Moreover, the optimal delta-v cost is only 7.4 m/s, which is orders of magnitude less than the delta-v capacity of current propulsion systems and only 10% of the cost of formation acquisition. This suggests that significantly larger integration times can be achieved, including margins for other operational constraints and contingencies. It is also noteworthy that the delta-v cost is very sensitive to errors in the inclination of the orbit. This behavior is expected because an error in the inclination changes the radial component of the pointing vector to the target at the apogee. However, the total delta-v cost of nominal operations will be less than the cost of formation acquisition if the inclination error is less than 0.75 deg. Also, the delta-v cost is nearly 100 times less sensitive to errors in the RAAN, as expected, because these errors change the along-track component of the pointing vector to the target. The difference between the simulated and reference costs ranges from 4.0 to 11.2 m/s across these simulations. Including the cost of formation acquisition (68.6 m/s), this difference represents 5–7% of the total delta-v cost of the mission. This demonstrates that errors in the dynamics model, measurements from the navigation sensors, and errors in the applied maneuvers have only a modest effect on the mission delta-v budget.

The sensitivity of the delta-v cost to errors in the argument of perigee of 1 deg or less was found to be negligible, and so these simulations were omitted from Table 8. Instead, a batch of simulations was conducted varying the reference argument of perigee from 0 to 360 deg. The simulated and reference costs for these scenarios are shown in Fig. 7. The trends in this plot clearly support the hypothesis

**Table 7 Key control law parameters used in simulations**

Parameter	Value
$\rho_{\perp,\max}$	0.20 m
$\rho_{\parallel,\max}$	200 m
$\dot{\rho}_{\perp,\max}$	0.02 m/s
$\epsilon_{\text{obs}}$	0.25
$\epsilon_{\text{control}}$	0.0167

**Table 8 Sensitivity of observation profile delta-v cost to absolute orbit errors for case study mission profile**

Error	$\Delta i$ , deg					$\Delta\Omega$ , deg				
	-1.0	-0.5	0	0.5	1.0	-1.0	-0.5	0	0.5	1.0
Simulation cost, m/s	94.4	48.8	7.4	47.7	91.0	8.5	7.9	7.4	7.5	8.2
Reference cost, m/s	83.2	42.4	3.4	39.6	80.3	4.3	3.7	3.4	3.7	4.3

from Sec. III that the optimal arguments of perigee are 90 and 270 deg and the worst-case arguments of perigee are 0 and 180 deg. Also, the proper choice of the argument of perigee reduces the delta-v cost by a factor of three, as compared to a worst-case choice.

The authors also conducted simulations to characterize the sensitivity of the delta-v cost to errors in inclination and the RAAN for a reference argument of perigee of 0 deg. It was found that the sensitivity to errors in inclination is 2.5 m/s per degree and the sensitivity to errors in the RAAN is 40 m/s per degree. These trends are reversed as compared to the results in Table 8, as expected, because errors in the RAAN affect the radial component of the pointing vector. These behaviors suggest that the optimal argument of perigee depends on the expected orbit injection error. If the orbit has an argument of perigee of 90 deg, then the delta-v cost will be minimized, provided that the inclination of the injected orbit is precisely controlled. However, this poses a risk because the inclination is nearly constant under the effects of perturbations in Earth orbit. It follows that it will be necessary to correct any error in inclination (at a cost of  $\sim$ 100 m/s per degree) or use more propellant to compensate for suboptimal formation alignment during observations. On the other hand, if the argument of perigee is 0 deg, then inclination errors of 1 deg have only a minor impact on the delta-v cost. In this case, it is critical to ensure that observations are performed near the optimal RAAN. Errors in the initial RAAN can be addressed at zero delta-v cost by properly timing mission operations to account for the precession due to  $J_2$ . Combining these results, the optimal argument of perigee is 90 or 270 deg if the orbit inclination provided by the launch vehicle can be controlled to better than 0.25 deg (from Table 8). If the inclination error is expected to be larger, the argument of perigee should be set at 0 or 180 deg to enable control of the radial component of the pointing vector to the target at zero delta-v cost through proper timing of observations.

It is also worthwhile to consider the evolution of the costs of individual mission phases over the mission lifetime. Figure 8 shows the evolution of the costs of individual observation phases (black) and reconfiguration phases (gray) for arguments of perigee of 90 deg (left) and 0 deg (right). The reference costs are indicated by dashed lines with x marks, and the simulated costs are indicated by solid lines with circles. The trends in these plots closely follow the expected

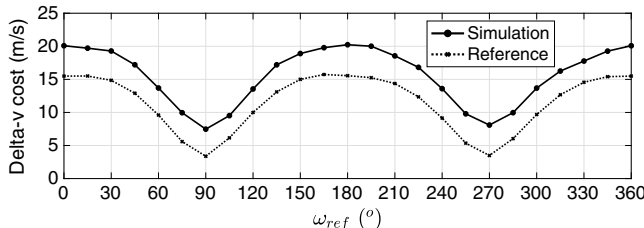


Fig. 7 Simulated and reference delta-v costs of observation profile vs reference argument of perigee.

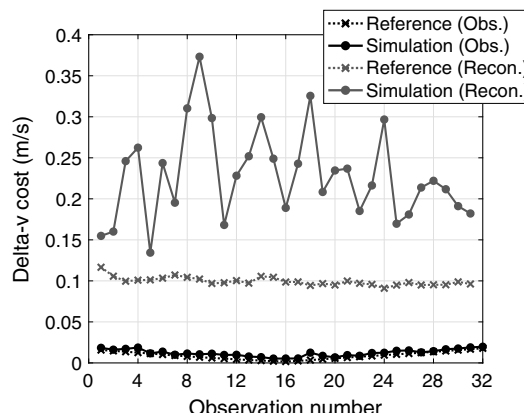


Fig. 8 Evolution of costs of individual mission phases for reference argument of perigee of 90 deg (left) and 0 deg (right) (Obs., observation; Recon., reconfiguration).

behaviors described in Sec. III. In the left-side plot, the pointing vector to the target evolves in the along-track direction, and so the cost of the observation phases varies slowly with time. The cost of the reconfiguration phases is nearly constant over the mission lifetime because the spacecraft always have equal orbit radii. In the right-side plot, the pointing vector to the target evolves in the radial direction, resulting in rapid changes in both the observation and reconfiguration phase costs due to the requirement of a nonzero difference in the semimajor axes during observations. Also, the costs are minimized in the middle of the mission lifetime, as expected, because this is when the formation is optimally aligned. Additionally, it is clear that the simulated and reference costs for observation phases are nearly identical, suggesting that the observation phase control law is nearly optimal. Instead, the simulated costs of the reconfiguration phases are generally 0.1–0.2 m/s higher than the reference cost. This behavior is not surprising because the reference cost assumes perfect dynamics and navigation knowledge throughout the orbit, whereas the simulations require rapid corrections near the end of the reconfiguration phases to ensure that the starshade reaches the control window. Although there is room for improvement in the control law (e.g., delaying the start of the observation phase when errors are large to save propellant), these measures will have little impact on the total delta-v budget unless extremely long integration times (hundreds of hours) are required.

Finally, it is instructive to consider the behavior of the control laws during the observation and reconfiguration phases. The trajectory during one observation phase of a mission profile with a reference argument of perigee of 90 deg and an inclination error of 0.5 deg is shown in Fig. 9. This simulation was selected to illustrate the behavior of the control law in the presence of nonnegligible lateral relative acceleration. The left-side plot shows the lateral relative position trajectory including the control window (dashed line), the region in which maneuvers are commanded according to Algorithm 1 (gray), and the locations of commanded maneuvers (circles). It is clear from this plot that the lateral relative position follows a parabolic trajectory after each maneuver with the vertex near the center of the control window. This behavior is consistent with the expected behavior from maneuvers commanded using Algorithm 1. Additionally, it is evident from the narrow parabolic trajectories that the executed maneuvers directly oppose the lateral relative acceleration, resulting in efficient control of the formation. Figure 9 (right) shows the evolution of the interspacecraft separation during the observation, including the 1% bounds (dashed lines). It is clear that the separation passively remains within 1% of the baseline at all times.

An example update step of the long-term control logic during the reconfiguration phase is shown in Fig. 10. For clarity, the update is shown in three different subspaces of the ROEs. In this plot, the current state estimate is indicated by a triangle, the propagated trajectory using the prior maneuver plan is shown as a solid line, and the  $3\sigma$  uncertainty ellipsoid surrounding the propagated state is shown in gray. It is evident that the desired state (indicated by a circle) is outside of the  $3\sigma$  ellipsoid in the relative inclination vector plane ( $\delta i_x$  and  $\delta i_y$ ), and so it is necessary to update the maneuver plan. The

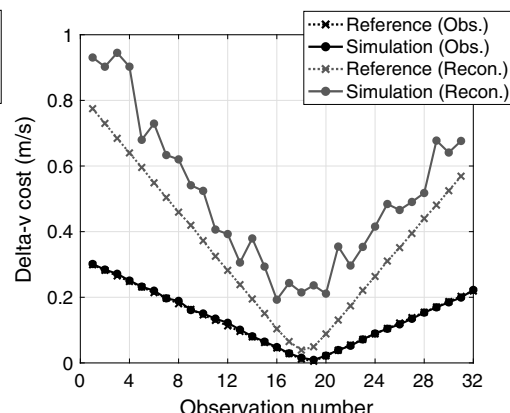
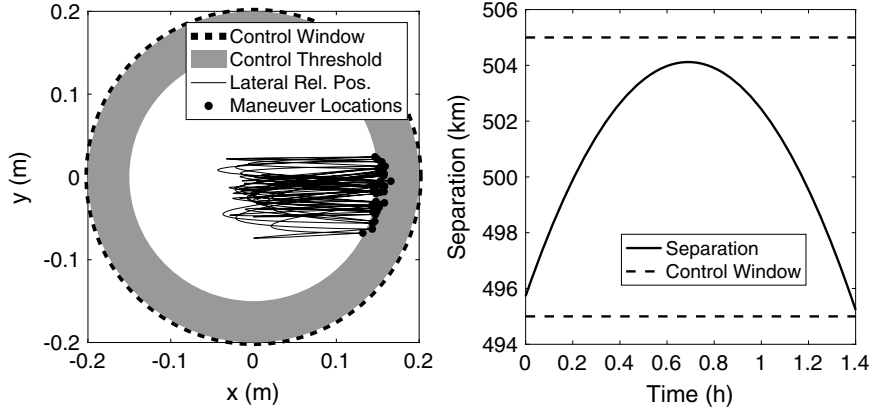
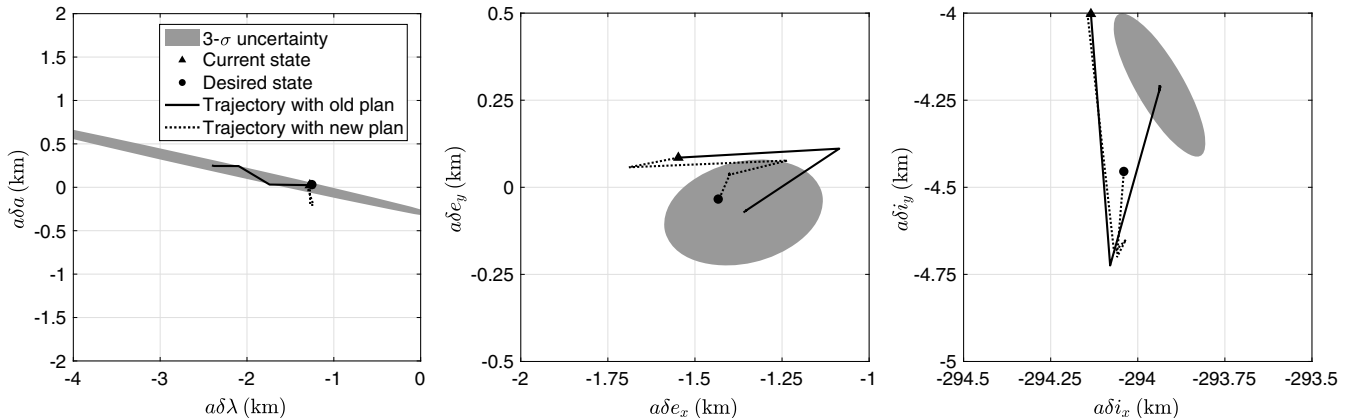


Fig. 8 Evolution of costs of individual mission phases for reference argument of perigee of 90 deg (left) and 0 deg (right) (Obs., observation; Recon., reconfiguration).



**Fig. 9** Evolution of lateral (right) and longitudinal (left) relative positions (Rel. Pos.) during observation phase including control windows (dashed lines), the region in which maneuvers are commanded (gray), and locations of executed maneuvers (circles).



**Fig. 10** Update of long-term control logic during reconfiguration.

propagated trajectory using the updated maneuver plan (dashed line) reaches the desired state. By repeating these updates over the reconfiguration phase, it is ensured that the formation will be properly aligned to within the precision of the navigation system, minimizing the delta-v required to reach the control window during the short-term control phase.

Overall, these results demonstrate that the proposed navigation and control architecture provides efficient and accurate control of the formation alignment, enabling repeated observations of scientifically interesting targets. Combined with the proposed formation design, it is possible to achieve tens to hundreds of hours of integration time for a specified target at low delta-v cost, enabling valuable science missions such as high-contrast imaging of exoplanets. Also, it is clear that the orbit design problem is well-understood because sensitivity of the delta-v cost to orbit errors follows all predicted trends.

## VI. Conclusions

This paper presents a new formation design that enables deployment of large distributed telescopes for astrophysics applications in Earth orbit. Within this context, this paper includes three contributions to the state of the art. First it is demonstrated that targets of scientific interest can be imaged using a 10- to 20-cm-aperture telescope and 1- to 5-m-diameter starshade. These systems require integration times on the order of minutes to image debris disks and tens of hours to image Jupiter analogs orbiting bright nearby stars. Second, optimal absolute and relative orbits that minimize the combined costs of periodic observations and formation reconfigurations including the effects of perturbations are derived in closed form. These orbit designs are based on the fundamental assumption that control is only applied perpendicular to the line of sight during observations to minimize the impact of the large relative accelerations in Earth orbit on the delta-v cost of the mission. It was found that the delta-v cost of repeated observations is minimized

by ensuring that the spacecraft have equal orbit radii and are aligned in the cross-track direction during observations. Third, a multistage navigation and control architecture is proposed to efficiently control the formation. This architecture uses a state-space logic during observations and a real-time optimal impulsive control solver to update the maneuver plan whenever the projected final state and covariance violate user-specified criteria during reconfigurations.

The performance and value of the proposed formation design were demonstrated through simulations of a reference mission to image the exoplanet AEgir using a small starshade and telescope. This mission and possible variants could be used to retire critical formation flying technology gaps and perform precursor science in service of future flagship missions. It was found that a formation in an optimal orbit can accumulate 44 h of integration time with a total delta-v cost as low as 7.4 m/s, excluding formation acquisition. The cost incurred by dynamics, navigation, and control errors was assessed by comparing the simulation results to ideal reference costs for each mission phase. It was found that these errors increase the delta-v cost of the mission by 4–11 m/s, with the majority of this difference incurred during reconfiguration phases. Also, the complete delta-v cost for the mission is under 100 m/s, which is easily achievable using current small satellite propulsion technologies.

Overall, the results presented in this paper demonstrate that the proposed formation design enables deployment of large distributed telescopes for astrophysics missions to be deployed in Earth orbit at low delta-v cost. This design can be used to reduce the cost of flagship missions that would otherwise have to be deployed in deep space and enable low-cost pathfinder missions to retire critical technology gaps and conduct precursor science.

## Acknowledgments

This work was supported by a NASA Office of the Chief Technologist Space Technology Research Fellowship, NASA grant

no. NNX15AP70H, and the King Abdulaziz City for Science and Technology. The authors would also like to thank the starshade team at the Jet Propulsion Laboratory for their help in developing the starshade manufacturing and deployment error budget. Previous version of this paper was presented as Paper 15-15 at the AAS/AIAA Astrodynamics Specialist Conference, Vail, CO, 9–13 August 2015.

## References

- [1] Castellani, L. T., Llorente, J. S., Ibarz, J. M. F., Ruiz, M., Mestreau-Garreau, A., Cropp, A., and Santovincenzo, A., "PROBA-3 Mission," *International Journal of Space Science and Engineering*, Vol. 1, No. 4, 2013, pp. 349–366.  
doi:10.1504/IJSPACESE.2013.059268
- [2] Cash, W., Shipley, A., Osterman, S., and Joy, M., "Laboratory Detection of X-Ray Fringes with a Grazing-Incidence Interferometer," *Nature*, Vol. 407, No. 6801, 2000, pp. 160–162.  
doi:10.1038/35025009
- [3] Seager, S., Turnbull, M., Sparks, W., Thomson, M., Shaklan, S. B., Roberge, A., Kuchner, M., Kasdin, N. J., Domagal-Goldman, S., Cash, W., et al., "The Exo-S Probe Class Starshade Mission," *Proceedings of SPIE 9605, Techniques and Instrumentation for Detection of Exoplanets VII*, Sept. 2015, Paper 96050W.
- [4] Lawson, P. R., Seager, S., Stapelfeldt, K., Brenner, M., Lisman, D., Siegler, N., Unwin, S., and Warfield, K., "An Analysis of Technology Gaps and Priorities in Support of Probe-Scale Coronagraph and Starshade Missions," *Space Telescopes and Instrumentation 2014: Optical, Infrared, and Millimeter Wave*, Vol. 9143, SPIE, Bellingham, WA, 2014.  
doi:10.1117/12.2054939
- [5] Ertel, S., et al., "The HOSTS Survey—Exozodiacal Dust Measurements for 30 Stars," *Astronomical Journal*, Vol. 155, No. 5, 2018, pp. 0–19.  
doi:10.3847/1538-3881/aab717
- [6] Sabol, C., Burns, R., and McLaughlin, C. A., "Satellite Formation Flying Design and Evolution," *Journal of Spacecraft and Rockets*, Vol. 38, No. 2, 2001, pp. 270–278.  
doi:10.2514/2.3681
- [7] D'Amico, S., Montenbruck, O., Arbinger, C., and Fiedler, H., "Formation Flying Concept for Close Remote Sensing Satellites," *15th AAS/AIAA Space Flight Mechanics Conference*, AAS Paper 05–156, Washington, D.C., 2005.
- [8] Hsiao, F. Y., and Scheeres, D. J., "Design of Spacecraft Formation Orbits Relative to a Stabilized Trajectory," *Journal of Guidance, Control, and Dynamics*, Vol. 28, No. 4, 2005, pp. 782–794.  
doi:10.2514/1.8433
- [9] Roscoe, C. W. T., Vadali, S. R., Alfriend, K. T., and Desai, U. P., "Optimal Formation Design for Magnetospheric Multiscale Mission Using Differential Orbital Elements," *Journal of Guidance, Control, and Dynamics*, Vol. 34, No. 4, 2011, pp. 1070–1080.  
doi:10.2514/1.52484
- [10] Landgraf, M., and Mestreau-Garreau, A., "Formation Flying and Mission Design for Proba-3," *Acta Astronautica*, Vol. 82, No. 1, 2013, pp. 137–145.  
doi:10.1016/j.actaastro.2012.03.028
- [11] Tillerson, M., and How, J. P., "Advanced Guidance Algorithms for Spacecraft Formation-Keeping," *Proceedings of the 2002 American Control Conference*, Vol. 4, American Automatic Control Council, Dover, Delaware, 2002, pp. 2830–2835.  
doi:10.1109/ACC.2002.1025218
- [12] D'Amico, S., and Montenbruck, O., "Proximity Operations of Formation-Flying Spacecraft Using an Eccentricity/Inclination Vector Separation," *Journal of Guidance, Control, and Dynamics*, Vol. 29, No. 3, 2006, pp. 554–563.  
doi:10.2514/1.15114
- [13] Koenig, A. W., and D'Amico, S., "Robust and Safe N-Spacecraft Swarming in Perturbed Near-Circular Orbits," *Journal of Guidance, Control, and Dynamics*, Vol. 41, No. 8, 2018, pp. 1643–1662.  
doi:10.2514/1.G003249
- [14] Bauer, F. H., Hartman, K., How, J. P., Bristow, J., Weidow, D., and Busse, F., "Enabling Spacecraft Formation Flying Through Spaceborne GPS and Enhanced Automation Technologies," *ION-GPS Conference*, Vol. 1, Inst. of Navigation, Manassas, VA, 1999, pp. 369–384.
- [15] Ardaens, J.-S., D'Amico, S., and Cropp, A., "GPS-Based Relative Navigation for the Proba-3 Formation Flying Mission," *Acta Astronautica*, Vol. 91, Oct.–Nov. 2013, pp. 341–355.  
doi:10.1016/j.actaastro.2013.06.025
- [16] Winternitz, L. B., Bamford, W. A., Price, S. R., Carpenter, J. R., Long, A. C., and Farahmand, M., "Global Positioning System Navigation Above 76,000 km for NASA's Magnetospheric Multiscale Mission," *Navigation: Journal of The Institute of Navigation*, Vol. 64, No. 2, 2017, pp. 289–300.  
doi:10.1002/navi.v64.2
- [17] Sullivan, J., and D'Amico, S., "Nonlinear Kalman Filtering for Improved Angles-Only Navigation Using Relative Orbital Elements," *Journal of Guidance, Control, and Dynamics*, Vol. 40, No. 9, 2017, pp. 2183–2200.  
doi:10.2514/1.G002719
- [18] Schaub, H., and Alfriend, K. T., "Hybrid Cartesian and Orbit Element Feedback Law for Formation Flying Spacecraft," *Journal of Guidance, Control, and Dynamics*, Vol. 25, No. 2, 2002, pp. 387–393.  
doi:10.2514/2.4893
- [19] Vadi, S. S., Alfriend, K. T., Vadali, S. R., and Sengupta, P., "Formation Establishment and Reconfiguration using Impulsive Control," *Journal of Guidance, Control, and Dynamics*, Vol. 28, No. 2, 2005, pp. 262–268.  
doi:10.2514/1.6687
- [20] Ardaens, J.-S., and D'Amico, S., "Control of Formation Flying Spacecraft at a Lagrange Point," German Aerospace Center (DLR)/German Space Operations Center TR 00-08, 2008.
- [21] Gaias, G., and D'Amico, S., "Impulsive Maneuvers for Formation Reconfiguration Using Relative Orbital Elements," *Journal of Guidance, Control, and Dynamics*, Vol. 38, No. 6, 2015, pp. 1036–1049.  
doi:10.2514/1.G000189
- [22] Roscoe, C. W. T., Westphal, J. J., Griesbach, J. D., and Schaub, H., "Formation Establishment and Reconfiguration Using Differential Elements in J2-Perturbed Orbits," *Journal of Guidance, Control, and Dynamics*, Vol. 38, No. 9, 2015, pp. 1725–1740.  
doi:10.2514/1.G000999
- [23] Scharf, D. P., Hadaegh, F. Y., and Ploen, S. R., "A Survey of Spacecraft Formation Flying Guidance and Control (Part 1): Guidance," *Proceedings of the 2003 American Control Conference*, SPIE, Bellingham, WA, 2003, pp. 1733–1739.  
doi:10.1109/ACC.2003.1239845
- [24] Scharf, D. P., Hadaegh, F. Y., and Ploen, S. R., "A Survey of Spacecraft Formation Flying Guidance and Control. Part II: Control," *Proceedings of the 2004 American Control Conference*, Inst. of Navigation, Manassas, VA, 2004, pp. 2976–2985.  
doi:10.23919/ACC.2004.1384365
- [25] Bandyopadhyay, S., Foust, R., Subramanian, G. P., Chung, S.-J., and Hadaegh, F. Y., "Review of Formation Flying and Constellation Missions Using Nanosatellites," *Journal of Spacecraft and Rockets*, Vol. 53, No. 3, 2016, pp. 567–578.  
doi:10.2514/1.A33291
- [26] Di Mauro, G., Lawn, M., and Bevilacqua, R., "Survey on Guidance Navigation and Control Requirements for Spacecraft Formation-Flying Missions," *Journal of Guidance, Control, and Dynamics*, Vol. 41, No. 3, 2018, pp. 581–602.  
doi:10.2514/1.G002868
- [27] Mennesson, B., Gaudi, S., Seager, S., Cahoy, K., Domagal-Goldman, S., Feinberg, L., Guyon, O., Kasdin, J., Marois, C., Mawet, D., et al., "The Habitable Exoplanet (HabEx) Imaging Mission: Preliminary Science Drivers and Technical Requirements," *Space Telescopes and Instrumentation 2016: Optical, Infrared, and Millimeter Wave*, Vol. 9904L, 2016.  
doi:10.1117/12.2240457
- [28] Crill, B. P., and Siegler, N., "Space Technology for Directly Imaging and Characterizing Exo-Earths," *UV/Optical/IR Space Telescopes and Instruments: Innovative Technologies and Concepts VIII*, Vol. 10398, SPIE, Bellingham, WA, 2017, Paper 103980H.  
doi:10.1117/12.2275697
- [29] Delpech, M., Malbet, F., Karlsson, T., Larsson, R., Léger, A., and Jorgensen, J., "Flight Demonstration of Formation Flying Capabilities for Future Missions (NEAT Pathfinder)," *Acta Astronautica*, Vol. 105, No. 1, 2014, pp. 82–94.  
doi:10.1016/j.actaastro.2014.05.027
- [30] Song, Y., Lee, Y. R., Park, J.-P., and Park, S.-Y., "CANYVAL-X: Operational Scenario and Strategy," *2018 SpaceOps Conference*, AIAA Paper 2018-2636, 2018.  
doi:10.2514/6.2018-2636
- [31] Koenig, A. W., and D'Amico, S., "Real-Time Algorithm for Globally Optimal Impulsive Control of Linear Time-Variant Systems," *IEEE Transactions on Automatic Control* (submitted for publication).
- [32] Peters, T. V., Branco, J., Escorial, D., Castellani, L. T., and Cropp, A., "Mission Analysis for PROBA-3 Nominal Operations," *Acta Astronautica*, Vol. 102, Sept.–Oct. 2014, pp. 296–310.  
doi:10.1016/j.actaastro.2014.01.010

- [33] Hatzes, A. P., Cochran, W. D., McArthur, B., Baliunas, S. L., Walker, G. A. H., Campbell, B., Irwin, A. W., Yang, S., Kürster, M., Endl, M., et al., "Evidence for a Long-Period Planet Orbiting Eridani," *Astrophysical Journal Letters*, Vol. 544, No. 2, 2000, pp. L145–L148.  
doi:10.1086/317319
- [34] Koenig, A. W., "Formation Design of Distributed Telescopes in Earth Orbit with Application to High-Contrast Imaging," Ph.D. Thesis, Stanford Univ., Stanford, CA, 2019.
- [35] Koenig, A. W., D'Amico, S., and Macintosh, B., "A Pareto-Optimal Characterization of Small-Scale Distributed Occulter/Telescope Systems," *SPIE Optics + Photonics*, SPIE, Bellingham, WA, 2015.
- [36] Cash, W., "Detection of Earth-like Planets Around Nearby Stars Using a Petal-Shaped Occulter," *Nature*, Vol. 442, No. 7098, 2006, pp. 51–53.  
doi:10.1038/nature04930
- [37] Vanderbei, R. J., Cady, E., and Kasdin, N. J., "Optimal Occulter Design for Finding Extrasolar Planets," *Astrophysical Journal*, Vol. 665, No. 1, 2007, pp. 794–798.  
doi:10.1086/509297
- [38] Harness, A., Cash, W., and Warwick, S., "High Contrast Observations of Bright Stars with a Starshade," *Experimental Astronomy*, Vol. 44, No. 2, 2017, pp. 209–237.  
doi:10.1007/s10686-017-9562-1
- [39] Bolcar, M. R., Balasubramanian, K., Crooke, J., Feinberg, L., Quijada, M., Rauscher, B. J., Redding, D., Rioux, N., Shaklan, S., Stahl, H. P., et al., "Technology Gap Assessment for a Future Large-Aperture Ultraviolet-Optical-Infrared Space Telescope," *Journal of Astronomical Telescopes, Instruments, and Systems*, Vol. 2, No. 4, 2016, Paper 041209.  
doi:10.1117/1.JATIS.2.4.041209
- [40] Glassman, T., Lo, A. S., Arenberg, J., Cash, W., and Noecker, C., "Starshade Scaling Relations," *SPIE Optical Engineering + Applications*, Vol. 7440, International Soc. for Optics and Photonics, Paper 744013, Bellingham, WA, 2009, Paper 744013.  
doi:10.1117/12.825033
- [41] Cash, W., "Analytic Modeling of Starshades," *Astrophysical Journal*, Vol. 738, No. 1, 2011, pp. 0–13.  
doi:10.1088/0004-637X/738/1/76
- [42] Cash, W., Schindhelm, E., Arenberg, J., Lo, A., Polidan, R., Kasdin, J., Vanderbei, R., Kilstrom, S., and Noecker, C., "External Occulters for Direct Observation of Exoplanets: An Overview," *UV/Optical/IR Space Telescopes: Innovative Technologies and Concepts III*, Vol. 6687, SPIE, Bellingham, WA, 2007.  
doi:10.1117/12.732645
- [43] Grant, M., and Boyd, S., "CVX: Matlab Software for Disciplined Convex Programming, Version 2.1," CVX Research, Inc., Austin, TX, Dec. 2018, <http://cvxr.com/cvx> [retrieved 06 Jan. 2018].
- [44] Grant, M., and Boyd, S., "Graph Implementations for Nonsmooth Convex Programs," *Recent Advances in Learning and Control*, Lecture Notes in Control and Information Sciences, Springer-Verlag, New York, pp. 95–110, 2008.  
doi:10.1007/978-1-84800-155-8-7
- [45] "Blue Canyon Technologies Nano Star Tracker (NST) Datasheet," <http://bluecanyontech.com/wp-content/uploads/2018/07/DataSheetStarTrackers07.pdf>.
- [46] D'Amico, S., "Autonomous Formation Flying in Low Earth Orbit," Ph.D. Thesis, Delft Univ. of Technology, Delft, The Netherlands, 2010.
- [47] Koenig, A. W., Guffanti, T., and Dmico, S., "New State Transition Matrices for Spacecraft Relative Motion in Perturbed Orbits," *Journal of Guidance, Control, and Dynamics*, Vol. 40, No. 7, 2017, pp. 1749–1768.  
doi:10.2514/1.G002409
- [48] Breger, L., and How, J. P., "Gauss's Variational Equation-Based Dynamics and Control for Formation Flying Spacecraft," *Journal of Guidance, Control, and Dynamics*, Vol. 30, No. 2, 2007, pp. 437–448.  
doi:10.2514/1.22649
- [49] D'Amico, S., Ardaens, J.-S., and Larsson, R., "Spaceborne Autonomous Formation-Flying Experiment on the PRISMA Mission," *Journal of Guidance, Control, and Dynamics*, Vol. 35, No. 3, 2012, pp. 834–850.  
doi:10.2514/1.55638
- [50] Giralo, V., and D'Amico, S., "Distributed Multi-GNSS Timing and Localization for Nanosatellites," *ION GNSS+*, Inst. of Navigation, Manassas, VA, 2018, pp. 2518–2534.  
doi:10.33012/2018.15979
- [51] Benedict, G. F., et al., "The Extrasolar Planet  $\epsilon$  Eridani b: Orbit and Mass," *Astronomical Journal*, Vol. 132, No. 5, 2006, pp. 2206–2218.  
doi:10.1086/508323
- [52] Giralo, V., and D'Amico, S., "Development of the Stanford GNSS Navigation Testbed for Distributed Space Systems," *Institute of Navigation, International Technical Meeting*, Inst. of Navigation, 2018, pp. 837–856.
- [53] Tapley, B. D., Bettadpur, S., Watkins, M., and Reigber, C., "The Gravity Recovery and Climate Experiment: Mission Overview and Early Results," *Geophysical Research Letters*, Vol. 31, No. 9, 2004, Paper L09607.  
doi:10.1029/2004GL019920
- [54] Picone, J. M., Hedin, A. E., Drob, D. P., and Aikin, A. C., "NRLMSISE-00 Empirical Model of the Atmosphere: Statistical Comparisons and Scientific Issues," *Journal of Geophysical Research: Space Physics*, Vol. 107, No. A12, 2002, pp. 15–16.  
doi:10.1029/2002JA009430

D. B. Spencer  
Associate Editor